The newly developed Multi-ensemble Biomass-burning Emissions Inventory (MBEI): Characterizing and unraveling spatiotemporal uncertainty in global biomass burning emissions

Xinlu Liu[1,2], Zhongyi Sun[2*], Chong Shi[1], Peng Wang[3], Tangzhe Nie[4], Qingnan Chu[5], Huazhe Shang[1], Lu Sun[6], Dabin Ji[1], Meng Guo[7], Kunpeng Yi[8], Zhenghong Tan[9], Lan Wu[2], Xinchun Lu[1,4], Shuai Yin[1*]

[1]State Key Laboratory of Remote Sensing and Digital Earth, Aerospace Information Research Institute, Chinese Academy of Sciences. Beijing 100101, China

[2]College of Ecology and Environment, Hainan University, Haikou 570228, China

[3]Department of Atmospheric and Oceanic Sciences, Fudan University, Shanghai, 200438, China

[4]School of Water Conservancy and Electric Power, Heilongjiang University, Harbin 150006, China

[5]Centro de Biotecnologia y Genómica de Planta (UPM-INIA). Universidad Politécnica de Madrid, Campus de Montegancedo, Madrid, Spain

[6]School of Human Settlements and Civil Engineering, Xi'an Jiaotong University, Shanxi Province, 710049, China

[7]School of Geographical Sciences, Northeast Normal University, Changchun 130024, China

[8]State Key Laboratory of Urban and Regional Ecology, Research Center for Eco-Environmental Sciences, Chinese Academy of Sciences, Beijing 100085, China

[9]School of Ecology and Environmental Science, Yunnan University, Kunming 650500, China

Correspondence to: Shuai Yin (yinshuai@aircas.ac.cn) and Zhongyi Sun (gis.rs@hainanu.edu.cn)

Abstract. Large discrepancies among existing inventories hinder a consensus on the true magnitude and long-term trends of global biomass burning emissions. To address this, we developed the Multi-ensemble Biomass-burning Emissions Inventory (MBEI), a framework integrating bottom-up and top-down approaches with multi-source data to generate eight sub-inventories for the period 2003–2023. This ensemble approach allows for the explicit quantification of emission uncertainty at a 0.1° grid scale. We estimate global annual CO_2 emissions at 7304 (4400–9657) Tg, with the maximum estimate exceeding the minimum by over two-fold. The uncertainty exhibits significant spatial heterogeneity: it is highest in low-emission regions like Australia and the Middle East (6.0–7.0 fold difference), whereas traditional hotspots like Africa show lower divergence (Approximately 2 fold). Temporally, a distinct decadal shift was identified: global emissions declined from 2003 to 2013 due to reduced tropical burning, but reversed to an increasing trend from 2013 to 2023, driven by intensified fires in northern high-latitudes and extreme events. Comparisons confirm that the MBEI mean provides a robust central estimate, while its max-min range effectively encompasses other major inventories. By providing explicit uncertainty bounds, MBEI enhances the reliability of atmospheric modeling and climate assessments. The dataset is publicly available at https://doi.org/10.5281/zenodo.18104830 (Liu and Yin, 2025).

1 Introduction

Biomass burning, encompassing forest fires, grassland fires, and the burning of agricultural residues, is a key disturbance in terrestrial ecosystems (Bowman et al., 2020; Jones et al., 2022). It profoundly influences local and global ecological processes and climate systems by releasing large quantities of greenhouse gases (GHGs) and aerosol particles (Bowman et al., 2009; Letu et al., 2023; Pellegrini et al., 2018; Shi et al., 2025; Yin, 2021). Accelerating climate change is driving significant shifts in the spatiotemporal patterns of global biomass burning, affecting its frequency, intensity, and duration. Observational data indicate that the incidence of extreme biomass burning events has increased 2.2-fold in the last two decades (Cunningham et al., 2024; Wang et al., 2023), and climate models project that high-risk areas for global biomass burning will expand by nearly one-third by the end of the 21st century (Senande-Rivera et al., 2022). Notably, while the burned area is shrinking in some traditional high-frequency burning regions (e.g., tropical rainforests) (Andela et al., 2017; Zheng et al., 2021), the fire-prone season is substantially extending. In regions such as southeastern Australia, eastern Siberia, and eastern North America, the length of fire weather season has increased by 27%–94%, significantly prolonging the period during which ecosystems are exposed to fire risk (Jones et al., 2022).

The increase of biomass burning frequency is raising atmospheric concentrations of GHGs, thereby exerting a strong perturbation on Earth's biospheric processes (Andreae, 2019; Andreae and Merlet, 2001; Yin et al., 2025). Between 1997 and 2016, global carbon emissions from biomass burning averaged 2.2 Pg C per year, equivalent to approximately 6% of global fossil fuel CO_2 emissions in 2014 (Friedlingstein et al., 2025; Liu et al., 2024; van der Werf et al., 2017). This increase in GHGs intensifies global warming, creating a feedback loop that is projected to elevate the risk of extreme fire weather by at least 50% in key regions such as western North America, equatorial Africa, Southeast Asia, and Australia by 2080 (Touma et al., 2021). Furthermore, particulate matter (e.g., black carbon, brown carbon, and organic carbon) emitted from biomass burning poses a serious threat to human health (Reid et al., 2005; Zhang et al., 2020). A meta-analysis of 81 studies (1980–2020) (Karanasiou et al., 2021). showed that exposure to $PM_{2.5}$ and PM_{10} from biomass burning is significantly associated with all-cause mortality, corresponding to a 1.31% (95% CI: 0.71–1.71) and 1.92% (95% CI: 1.19–5.03) increase for every 10 μg m^{-3} rise in PM_{10} and $PM_{2.5}$. These effect sizes exceed typical estimates for all-source ambient particulate matter, indicating that biomass burning PM may pose greater health risks than general ambient PM. From

1990 to 2019, $PM_{2.5}$-related excess mortality in equatorial Asia increased threefold, with approximately 317 thousand of these deaths attributed to high-intensity biomass burning from Indonesian peatlands (Yin, 2023).

Establishing high-precision emission inventories is crucial for assessing the impacts of biomass burning on the global atmospheric environment and public health (Bray et al., 2021; Filonchyk et al., 2024; Ramanathan and Carmichael, 2008). Trace gases and aerosols released by biomass burning not only affect global climate but also alter regional atmospheric chemistry via transboundary transport (Andreae, 2019). Atmospheric Chemistry Transport Models, which are used for air quality forecasting and source apportionment, rely on emission inventories with high spatiotemporal resolution and reliability. Such data are crucial for accurately resolving pollutant transport and transformation pathways, as well as for quantifying their contributions to pollution (Matthias et al., 2018; Wang et al., 2014). Currently, the construction of global and regional biomass burning emission inventories primarily relies on two established estimation pathways, the bottom-up and top-down approach. The bottom-up approach typically estimates emissions based on satellite-derived burned area (e.g., MODIS MCD64A1) combined with fuel load, combustion completeness, and emission factors (van der Werf et al., 2017; Wiedinmyer et al., 2023). The typical inventories of this approach include the Global Fire Emissions Database (GFED) and the Fire INventory from NCAR (FINN) (Giglio et al., 2006). In contrast, the alternative top-down approach estimates emissions based on Fire Radiative Power (FRP) retrieved from satellites in thermal infrared bands. This method utilizes the relationship between the time-integrated FRP, known as Fire Radiative Energy (FRE), and the total dry matter consumed, a relationship often calibrated using field observations (Ichoku and Ellison, 2014; Wooster et al., 2005). It estimates emissions by fitting the combustion curve of dry matter consumption derived from satellite-retrieved FRP (Santoro, 2018). The typical inventories include the Global Fire Assimilation System (GFAS) and the Quick Fire Emissions Dataset (QFED) (Andela et al., 2015; Giglio et al., 2020).

Although these two methods provide clear theoretical frameworks, their practical implementation varies among researchers in their choice of data sources, parameters, and algorithmic details, leading to significant discrepancies in the resulting inventories (Hoelzemann et al., 2004; Ichoku and Kaufman, 2005; Ito and Penner, 2004; Zhang et al., 2014). Consequently, estimates of total emissions for the same region or period can differ considerably (N'Datchoh et al., 2025; Pereira et al., 2016; Shi and Matsunaga, 2017; Whitburn et al., 2015). This discrepancy poses a key challenge in the field, as it not only directly

impacts the accuracy of atmospheric chemistry simulations and climate effect assessments (Liu et al., 2020; Longo et al., 2010; Stroppiana et al., 2010; Williams et al., 2012) but also leads to a lack of clear consensus on the true magnitude and long-term trends of global biomass burning emissions.

A growing body of evidence suggests that under the dual threats of climate change and human activities, the spatial distribution of global biomass burning is undergoing significant shifts. Fire activity is weakening in some traditional tropical hotspots (e.g., African savannas) while intensifying in high-latitude boreal forests (Tyukavina et al., 2022; van Wees et al., 2021; Yin et al., 2020b; Zheng et al., 2021, 2023). These complex and opposing regional trends obscure the long-term trajectory of global total emissions. In this context, the limitation of emission inventories, which provide only a single estimate, becomes more prominent. A single value cannot capture the extent to which observed regional trends reflect genuine physical processes versus mere algorithmic artifacts of a particular inventory. Therefore, accurately assessing the current state of biomass burning emissions requires not only improving the precision of inventories but also developing new methods to systematically quantify their uncertainty.

To address this challenge, we constructed the Multi-ensemble Biomass-burning Emissions Inventory (MBEI), a global biomass burning emission dataset for 2003–2023, by integrating mainstream top-down and bottom-up algorithms. This ensemble approach incorporates two fire-detection products and four sets of key input variables, resulting in eight distinct sub-inventories that quantify emissions for 11 key species (e.g., CO_2, $PM_{2.5}$, BC, and NO_2). By analyzing the mean and the maximum-minimum range (hereafter referred to as the "Max-Min band") of these eight sub-inventories, our study provides a new quantitative estimate of global biomass burning emissions over the past 21 years and, crucially, reveals their uncertainty across various spatial scales. It offers quantitative evidence to better interpret the shifts in global biomass burning patterns. The advantages of this new inventory allow data users (such as atmospheric chemistry modelers and climate assessment experts) to directly incorporate the variability of emission estimates into their analytical frameworks, thereby providing critical data support for dissecting complex global biomass burning dynamics and enhancing the robustness of their assessment results.

2 Materials and Methods

2.1 Datasets

The MBEI integrates two established methodologies: a bottom-up approach based on burned area and a top-down approach based on FRP (Vermote et al., 2009; Wiedinmyer et al., 2006). Active fire detections were sourced from the MODIS Near-Real-Time product (MCD14DL). To assess uncertainty stemming from detection confidence, we created two parallel processing streams using fire pixels from both Aqua and Terra satellites (2003–2023): one including all detected fires, and another restricted to fires with medium-to-high confidence (>30%). In addition, we introduced combination in key input variables: the bottom-up algorithm was driven by two alternative aboveground biomass (AGB) datasets (Biomass_cci and GlobBiomass), while the top-down algorithm utilized two different biome maps (8-class and 30-class) to define emission coefficients. For consistency, all input datasets were resampled to a common 0.1° spatial resolution and monthly temporal resolution. A comprehensive list of the datasets used in this study is provided in Table 1.

184 **Table 1. Datasets used in this study.**

Data types	Name	Temporal Coverage	Spatial Resolution	Temporal Resolution	Reference
Active Fire Data	Aqua MCD14DL	2003-2023	1 km × 1 km	daily	(NASA VIIRS Land Science Team, 2021)
	Terra MCD14DL	2003-2023	1 km × 1 km	daily	(NASA VIIRS Land Science Team, 2021)
Burning Efficiency (BE) & Emission Factor (EF) Data	EF Classification Source Data GFED	\	0.25° × 0.25°	\	(van der Werf et al., 2006)
	EF Coefficients	\	\	\	(van der Werf et al., 2017)
	BE Coefficients	\	\	\	(Shi et al., 2015)
AGB Data	GlobBiomass	2010	25 m × 25 m	\	(Santoro, 2018)
	Biomass_cci	2010/2015-2021	100 m × 100 m	yearly	(Santoro and Cartus, 2024)
Conversion Factor (CR) Data	30-class CR map	\	0.1° × 0.1°	\	(Kaiser et al., 2023)
	8-class CR map	\	0.1° × 0.1°	\	(Kaiser et al., 2012)
Ancillary & Validation Data	Net Primary Production (NPP) MYD17A3HGF v061	2003-2023	500 m × 500 m	yearly	(Running and Zhao, 2021)
	Land Cover Type MCD12Q1.061	2003-2023	500 m × 500 m	yearly	(Friedl and Sulla-Menashe, 2022)
Validation Inventory Data	Global Fire Emissions Database 5 (GFED 5)	2003-2022	0.25° × 0.25°	daily	(Binte Shahid et al., 2024; Vernooij et al., 2023; Wiggins et al., 2021)
	Fire INventory from NCAR 2.5 (FINN 2.5) MODIS	2002-2022	0.1° × 0.1°	daily	(Wiedinmyer et al., 2023)
	Global Fire Assimilation System 1.2 (GFAS 1.2)	2003-2022	0.1° × 0.1°	daily	(Kaiser et al., 2012)
	Quick Fire Emissions Dataset 3.1 (QFED 3.1)	2003-2022	0.1° × 0.1°	daily	(Koster et al., 2015)

185 Note: The 8-class biome map is derived from the 30-class biome map. See Fig. S1 for its spatial
186 distribution.

2.1.1 Active fire detection and fire radiative power

The sourced active fire data were obtained from the MODIS Near-Real-Time active fire product (MCD14DL C6.1), provided by NASA's Fire Information for Resource Management System (FIRMS). This product provides fire detections from both the Terra and Aqua satellites based on the MOD14/MYD14 thermal anomalies algorithm (Giglio et al., 2006). Each active fire detection represents the center of a 1-km pixel flagged as containing one or more fires.

For the period 2003–2023, we extracted daily fire locations, detection confidence, and FRP values. These 1-km daily data were then aggregated into monthly 0.1° grids, which form the primary input for both our top-down and bottom-up frameworks.

2.1.2 Burning efficiency and emission factor

To assign region- and vegetation-specific BE and EF, we first utilized the annual 500-m MODIS Land Cover Type product (MCD12Q1 C6.1), adopting its International Geosphere-Biosphere Programme (IGBP) classification scheme. We then assigned a BE value to each of the 17 IGBP classes using coefficients derived from Mieville et al. (2010) and Shi et al. (2015), with the specific values detailed in Table S3.

Emission factors were assigned by intersecting the MCD12Q1 land cover map with the 14 continental-scale regions defined by GFED (van der Werf et al., 2017). This process yielded a unique EF for each landcover region combination, allowing us to estimate emissions for 11 key atmospheric emission species as detailed in Table S4.

2.1.3 Aboveground biomass

To quantify available fuel load for the bottom-up framework and assess related uncertainties, we employed two independent global AGB datasets. The GlobBiomass provides a global AGB map at 25-m spatial resolution for the baseline year 2010, generated by synergistically fusing multi-source data, including observations from spaceborne Synthetic Aperture Radar (SAR), Light Detection and Ranging (LiDAR), and optical remote sensing, together with forest inventory data (Santoro, 2018). Biomass_cci, provided by the European Space Agency Climate Change Initiative (ESA CCI) project, contains global AGB maps at 100-m resolution for multiple years (2010, 2017, 2018, and annually for 2019–2021) (Mariani et al., 2016).

2.1.4 Conversion factor

In the top-down method, satellite-derived FRE, which is the temporal integral of FRP, is converted into the mass of combusted dry matter. This conversion is performed using a biome-specific conversion factor (kg Dry Matter MJ^{-1}). To assess the uncertainty associated with this parameter, we implemented two distinct sets of conversion factors: one based on the 8 major biomes used in the GFAS (Kaiser et al., 2012), and another based on a more detailed 30-class biome map. The spatial distributions and respective CR values for these two schemes are detailed in Figs. S1–S2 and Tables S1–S2.

2.1.5 Ancillary and validation data

To derive a dynamic annual AGB time series for 2003–2022 from otherwise static AGB maps, we used the MODIS annual Net Primary Production product MYD17A3HGF v061, which provides global NPP at 500 m spatial resolution. We leveraged the empirically supported linear relationship between NPP and AGB to temporally extrapolate the baseline AGB maps and generate annual AGB maps, with the detailed procedure and parameterization described in Section 2.2.1.

To evaluate the performance and robustness of the new inventory, we conducted a comprehensive intercomparison with four widely used global emission products that span both bottom-up and FRP methodologies. For the bottom-up approach, GFED 5.0 serves as a key benchmark, as its reliance on the Carnegie–Ames–Stanford Approach (CASA) biogeochemical model for fuel load estimation allows for a critical assessment of how a model-driven workflow differs from our use of direct remotely sensed AGB. To specifically isolate the influence of parameter choices (e.g., emission factors and burning efficiency), we included FINN 2.5 in our analysis. Because it is built upon the same MODIS active fire and land cover inputs, a comparison with FINN 2.5 provides a controlled setting to evaluate the impact of our system's unique parameterization. For the top-down FRP-based approach, GFAS 1.2 provides a reference for evaluating the plausibility of the combustion-rate coefficient schemes tested in this study, as it converts satellite-observed FRP to dry matter combusted in a manner consistent with our framework. Finally, we incorporated QFED 3.1, which represents an optimized evolution of GFAS applying more advanced correction and gap-filling procedures, to examine how alternative imputation strategies for missing FRP retrievals affect the spatiotemporal completeness of the final emission estimates.

2.2 The framework for the MBEI

To quantify global biomass burning emissions and their associated uncertainties, we constructed the MBEI using a multi-source ensemble framework. Unlike conventional approaches that rely on a single algorithm, this framework operates by generating an ensemble of eight independent sub-inventories (see Table 2). This design is explicitly structured to capture the structural uncertainty stemming from the fundamental mechanistic discrepancies between bottom-up (burned area-based) and top-down (fire radiative power-based) methodologies. Rather than obscuring these differences through data fusion, the MBEI leverages them to define the uncertainty bounds of the estimates. Consequently, for each 0.1° grid cell, we provide the ensemble mean as the central estimate, while delineating the uncertainty envelope through two metrics: the standard deviation, representing dispersion, and the maximum and minimum bounds, defining the uncertainty range. The overall workflow is illustrated in Fig. 1.

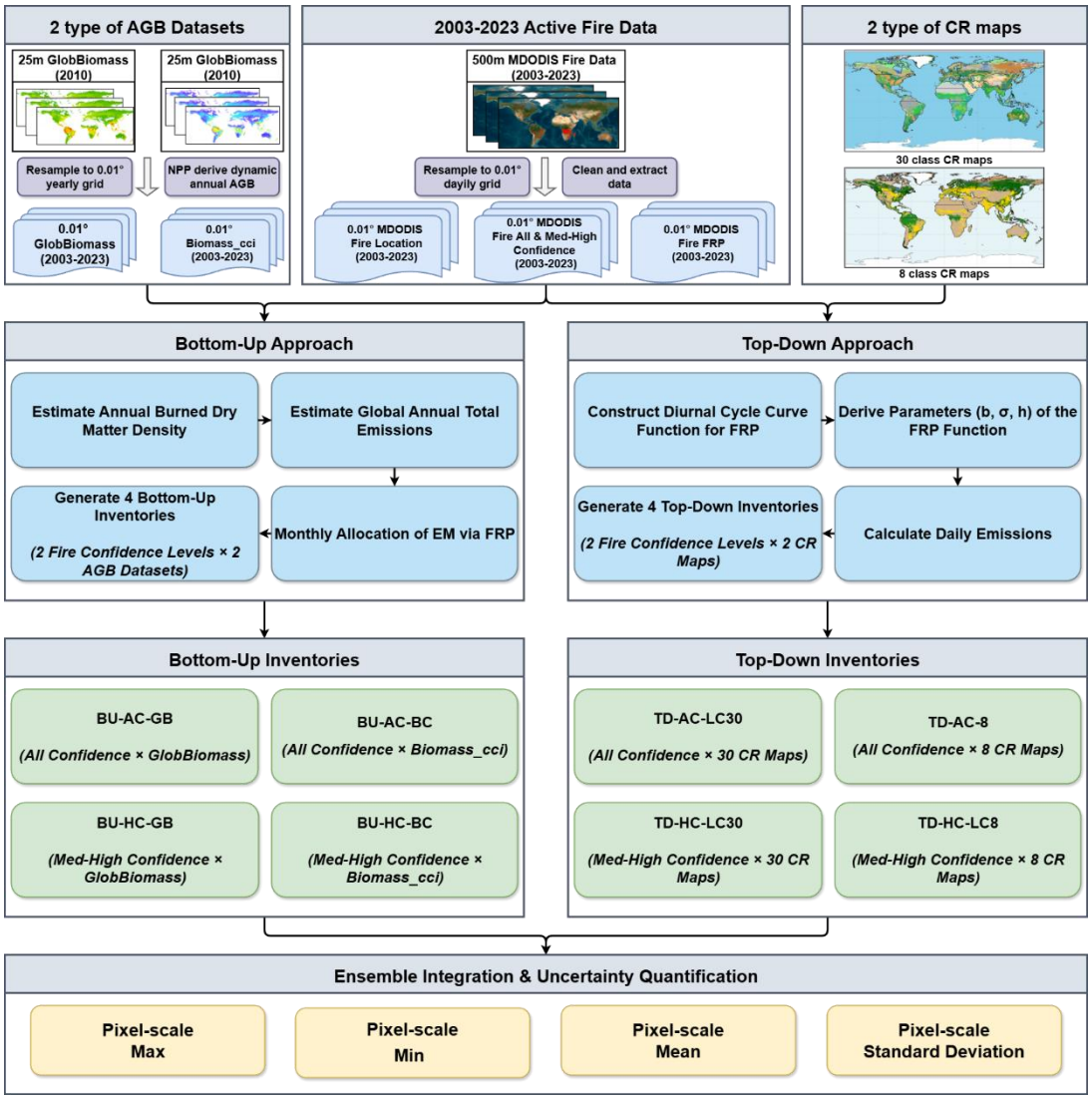

Figure 1. Framework for the construction of MBEI.

Table 2. The details of the eight biomass burning emission sub-inventories.

4 Bottom-Up Inventories			4 Top-Down Inventories		
Name	Confidence Level	Datasets	Name	Confidence Level	Datasets
BU-AC-GB	All Confidence	GlobBiomass	TD-AC-LC30	All Confidence	30-class CR map
BU-AC-BC	All Confidence	Biomass_cci	TD-AC-LC8	All Confidence	8-class CR map
BU-HC-GB	Medium-to-High confidence	GlobBiomass	TD-HC-LC30	Medium-to-High confidence	30-class CR map
BU-HC-BC	Medium-to-High confidence	Biomass_cci	TD-HC-LC8	Medium-to-High confidence	8-class CR map

Note: The final MBEI dataset also includes the pixel-level ensemble statistics (Mean, Std, Max, Min) calculated from these eight sub-inventories.

2.2.1 Bottom-up emission estimation

This study employs a bottom-up method, combining multi-source remote sensing data to construct four global monthly biomass burning emission inventories for 2003–2023. The core computational workflow involves four key steps: (1) constructing a dynamic annual AGB dataset based on interannual variations in NPP; (2) modeling the total burned dry matter density (BD) under multiple fire events within a year; (3) estimating total annual emissions (EM) by burned area (BA), BD and EF; (4) downscaling annual emissions to a monthly resolution using the monthly distribution of FRP.

To overcome the limitation of using a static AGB benchmark map that ignores interannual variability, we constructed a dynamic annual AGB dataset. Based on the ecological assumption of a stable proportional relationship between AGB and NPP (Raich et al., 2006; Whittaker and Likens, 1972), we used the relative interannual changes in the MODIS annual NPP product to extrapolate the baseline AGB. The AGB for a target year (m) in a specific pixel (p) is calculated as:

$$\mathrm{AGB}_{(m,p)} = \mathrm{AGB}_{(a,p)} \times \frac{\mathrm{NPP}_{(m,p)}}{\mathrm{NPP}_{(a,p)}} \quad (1)$$

where $\mathrm{AGB}_{(m,p)}$ is the AGB in year m at pixel p (Mg ha^{-1}); $\mathrm{AGB}_{(a,p)}$ is the baseline AGB at pixel p (mean of 2003–2023, Mg ha^{-1}); $\mathrm{NPP}_{(m,p)}$ is the NPP in year m at pixel p (kg C m^{-2} yr^{-1}); and $\mathrm{NPP}_{(a,p)}$ is the baseline mean NPP at pixel p (kg C m^{-2} yr^{-1}).

After obtaining annual AGB, we estimated the annual BD per unit area. Considering that a pixel may experience multiple fires in a year, we used the following model to simulate the sequential consumption of AGB by fire and accumulate the total annual burned amount:

$$BD_{(m,p)}=\sum_{j=1}^{I}\{AGB_{(m,p)}\times\ (1\text{-}BE_c)^{j\text{-}1}\times BE_c\} \quad (2)$$

where $BD_{(m,p)}$ is the total burned dry matter density in year m at pixel p (kg m^{-2}); I is the fire frequency in year m at pixel p (derived from active fire data); j represents the j-th fire event of the year; $AGB_{(m,p)}$ is the initial AGB at the beginning of the year (kg m^{-2}); and BE_c is the dimensionless burning efficiency for the land cover type c of pixel p (derived from the Land Cover Type MCD12Q1.061).

The total annual emissions of each pollutant are estimated based on the method proposed by Seiler and Crutzen (1980):

$$EM_{(m,p)} = BA_{(m,p)} \times BD_{(m,p)} \times EF \quad (3)$$

where $EM_{(m,p)}$ is the annual emission of a specific pollutant in year m at pixel p (g); $BA_{(m,p)}$ is the total annual burned area in year m at pixel p (m^2), obtained by multiplying the annual MODIS active fire location mask by the pixel's geographic area to ensure that the burned location is consistent with fire detections; $BD_{(m,p)}$ is the annual burned dry matter density (kg m^{-2}) calculated from Eq. (2); and EF is the emission factor for the specific pollutant (g kg^{-1}). It is important to note that inputs with annual temporal resolution (e.g., AGB, Land Cover-derived BE and EF) determine the magnitude of $EM_{(m,p)}$ in this step and are not interpolated.

Finally, to obtain a monthly-resolution emission inventory, we applied a temporal allocation approach. We used satellite-observed FRP as a high-frequency proxy for fire activity intensity to distribute the total annual emissions $EM_{(m,p)}$ into each month (t):

$$EM_{(m,p,t)}=EM_{(m,p)}\times\frac{FRP_{(m,p,t)}}{\sum_{t=1}^{12}FRP_{(m,p,t)}} \quad (4)$$

where $EM_{(m,p,t)}$ is the pollutant emission in month t of year m at pixel p (g); and $FRP_{(m,p,t)}$ is the monthly cumulative FRP in month t of year m at pixel p (MJ s^{-1}). This method ensures that while the total emission magnitude is constrained by annual fuel loads, the seasonality is driven by real-time fire radiative observations.

2.2.2 Top-down emission estimation

Our top-down emission estimation is based on the FRP approach, which uses satellite-observed thermal radiation to quantify biomass burning. The entire computational framework revolves around FRE, with the final pollutant emissions calculated as:

$$EM_{(p)} = FRE_{(p)} \times CR_{(r)} \times EF \quad (5)$$

where $EM_{(p)}$ is the daily emission at pixel p (g); $FRE_{(p)}$ is the daily cumulative FRE at pixel p (MJ); $CR_{(r)}$ is the conversion factor for the biome r where pixel p is located (kg Dry Matter MJ^{-1}); and EF is the emission factor for the specific pollutant (g kg^{-1}).

However, polar-orbiting satellites like MODIS provide only limited observations per day, making it impossible to obtain daily cumulative FRE by simple integration of instantaneous FRP. To overcome this, we reconstruct the FRP diurnal cycle by fitting a Gaussian function, following the methodology of Vermote et al. (2009). We assume that the diurnal variation of FRP for a single biomass burning event can be represented by a Gaussian function:

$$FRE_{(p)} = \int_0^{24} FRP(t)_{(p)}\,dt = \int_0^{24} FRP_{peak(p)} \left(b + e^{-\frac{(t-h)^2}{2\sigma^2}} \right) dt \quad (6)$$

where $FRP(t)_{(p)}$ is the instantaneous FRP at local time t for pixel p; $FRP_{peak(p)}$ is the peak FRP of the fire event at pixel p (MJ s^{-1}); h is the local time of peak FRP hours; σ is the standard deviation of the Gaussian function, characterizing energy release concentration of the fire; and b is a background term reflecting residual or background radiation during non-active burning periods. The Gaussian parameters b, σ, and h are empirically derived for each biome from the long-term mean FRP ratio between Terra and Aqua observations using the relationships (henceforth $\frac{\overline{FRP}_{Terra}}{\overline{FRP}_{Aqua}}$):

$$b = 0.86 \times \left(\frac{\overline{FRP}_{Terra}}{\overline{FRP}_{Aqua}} \right)^2 - 0.52 \times \frac{\overline{FRP}_{Terra}}{\overline{FRP}_{Aqua}} + 0.08 \quad (7)$$

$$\sigma = 3.89 \times \frac{\overline{FRP}_{Terra}}{\overline{FRP}_{Aqua}} + 1.03 \quad (8)$$

$$h = -1.23 \times \frac{\overline{FRP}_{Terra}}{\overline{FRP}_{Aqua}} + 14.57 \quad (9)$$

where $\overline{FRP}_{Terra}$ and $\overline{FRP}_{Aqua}$ are the long-term mean FRP values for the respective sensors within that biome (MJ s^{-1}).

316 The final FRP_{peak} is determined by selecting either the daily peak FRP from the Aqua satellite (henceforth
317 $FRP_{Aqua\ peak}$) or the daily peak FRP from the Terra satellite after correction with Eq. (12) (henceforth
318 FRP_{Terra_corr}):

$$FRP_{Aqua\ peak_{(p)}} = \frac{FRP_{Aqua(p)}}{\left(b+e^{-\frac{(1.5-h)^2}{2\sigma^2}}\right)+\left(b+e^{-\frac{(13.5-h)^2}{2\sigma^2}}\right)} \quad (10)$$

$$FRP_{Terra\ peak_{(p)}} = \frac{FRP_{Terra\_corr(p)}}{\left(b+e^{-\frac{(1.5-h)^2}{2\sigma^2}}\right)+\left(b+e^{-\frac{(13.5-h)^2}{2\sigma^2}}\right)} \quad (11)$$

$$FRP_{Terra\_corr(p)} = FRP_{Terra(p)} \times \frac{\overline{FRP}_{Terra}}{\overline{FRP}_{Aqua}} \quad (12)$$

319 where $FRP_{Terra\_corr(p)}$ is the corrected Terra FRP at pixel p (MJ s^{-1}), FRP_{Peak} was calculated from Aqua
320 satellite data using Eq. (10), following the approach of Vermote et al. (2009). Additionally, FRP values
321 from the Terra satellite were adjusted using Eq. (12). This adjustment utilized long-term FRP ratios for
322 different biomes to normalize the morning Terra observations to the afternoon measurement time of the
323 Aqua satellite.
324 Independent daily FRE estimates were then calculated using the original Aqua observations (FRP_{Aqua}
325 $_{peak(p)}$) and the corrected Terra observations ($FRE_{Terra\ peak(p)}$) in Eq. (6) at pixel p (MJ s^{-1}). The final daily
326 FRE is the average of these two estimates:

$$FRE_{(p)} = \frac{FRE_{Aqua(p)}+FRE_{Terra(p)}}{2} \quad (13)$$

327 Through these steps, we obtained the final daily FRE data. We then used Eq. (5) to calculate emissions
328 and aggregated them to a monthly scale, ultimately producing four independent top-down emission
329 inventories.

330 **2.3 Trend analysis**

331 Long-term trends in biomass burning emissions (2003–2022) were quantified using the Theil-Sen median
332 trend estimator, with statistical significance assessed by the Mann-Kendall (MK) test (Mann, 1945; Sen,
333 1968). This non-parametric approach is particularly suitable for geophysical time series like emission
334 data, as it is robust to outliers and does not assume a normal distribution.
335 The Theil-Sen estimator calculates the median of the slopes between all pairs of data points in the time
336 series, making it robust to outliers (e.g., emission peaks from extreme fire years) and providing a stable
337 estimate of the long-term trend. The slope is calculated as:

$$\text{slope}=\text{median}\frac{x_j-x_i}{j-i}\ (1\le i<j\le n) \quad (14)$$

where slope is the estimated trend, x_i and x_j are the data values at time points i and j, and n is the length of the time series.

3 Results

3.1 Spatial patterns and uncertainty of global biomass burning emissions

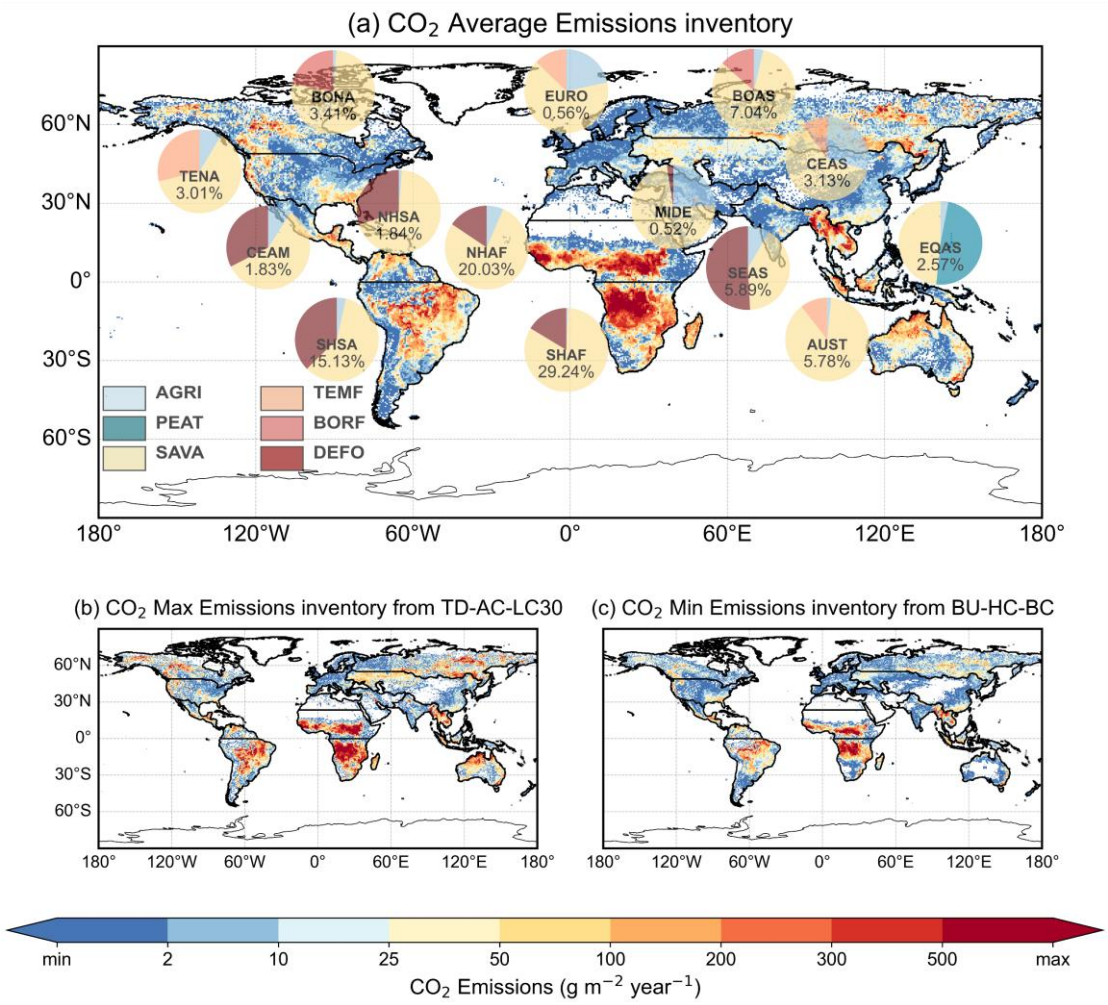

Figure 2. Spatial patterns and regional composition of global biomass burning CO_2 emissions (mean of 2003–2023). (a) Spatial distribution of the annual mean CO_2 emission flux estimated from the mean of the eight inventories in this study. The embedded pie charts show the emission composition for 14 major regions, where: 1) the number in the pie chart indicates the percentage of that region's emissions relative to the global total; and 2) the sectors of the pie chart represent the proportional contribution of six major fire types to the region's total emissions. (b) and (c) show the spatial emission patterns corresponding to the inventory with the highest global total annual emissions (TD-AC-LC30) and the lowest global total annual emissions (BU-HC-BC) among the eight inventories over the entire study period, respectively.

CO_2 is a principal greenhouse gas and the most widely studied species in biomass-burning inventories; accordingly, Sections 3.1–3.4 focus on CO_2, and results for other species are provided in the Supplementary Information. For 2003 to 2023, the framework-mean global annual emissions for all species are summarized in Table 3 and Table S5 The framework-mean CO_2 emission is 7303.63 Tg yr^{-1}, and the associated uncertainty, quantified as the range of annual means across the eight sub-inventories in the ensemble, spans 4400.08 to 9656.89 Tg yr^{-1}.

Fig. 2 shows the highly heterogeneous spatial pattern of mean annual CO_2 emission fluxes (the spatial patterns for other major pollutants are presented in Fig. S6). Global emission activities are largely concentrated in tropical and subtropical regions, characterized by high emission fluxes (> 300 g m^{-2} yr^{-1}). Within these areas, the most intense emission hotspots (> 500 g m^{-2} yr^{-1}) are clearly identified over the Congo Basin, surrounding savannas, and parts of Southern Africa. This high spatial concentration of intense burning directly translates to Africa's dominant role in the global emission budget. Based on regional statistics (Global 14 regions defined in Fig. S3), Southern Hemisphere South Africa (SHAF) and Northern Hemisphere South Africa (NHAF) collectively contribute 49.2% of global CO_2 emissions (29.2% and 20.0%, respectively). Furthermore, Southern Hemisphere South America (SHSA, 15.1%), Boreal Asia (BOAS, 7.0%), and Southeast Asia (SEAS, 5.9%) also stand out as major source regions for global biomass burning.

The dominant types of biomass burning vary substantially by region (see Fig. S4 for the classification of fire types), leading to distinct emission profiles (see Fig. S5 for the composition of fire types in each region). In the top three emitting regions (SHAF, NHAF, and SHSA), which collectively account for nearly two-thirds (64.4%) of global CO_2 emissions, burning is driven primarily by savanna fires (SAVA) and deforestation fires (DEFO). The contribution of different fire types varies significantly among these top regions (see Fig. 2a for detailed emission values). In SHAF, the largest source, SAVA are overwhelmingly dominant, accounting for 83% of its CO_2 emissions. A similar pattern occurs in NHAF, where SAVA contributes 78% of emissions, although agricultural waste burning (AGRI) also plays a notable role (6%). In contrast, the emissions in SHSA are more evenly split between SAVA (59%) and DEFO fires (37%). In the high-latitude regions of BOAS and Boreal North America (BONA), fires in boreal forests (BORF) are a characteristic emission source, contributing 14% and 22% of regional CO_2 emissions, respectively. Notably, our analysis identifies fires classified as SAVA as the largest contributor

in both regions (83% in BOAS and 77% in BONA). It is critical to note that SAVA in this context refers to the burning of extensive grasslands and shrublands located within the boreal climate zone, as defined by our underlying land cover dataset, rather than tropical savannas. This highlights that non-forest fires are the dominant source of emissions even in these high-latitude zones.

The emission composition of Equatorial Asia (EQAS) is unique. Although its total emissions are relatively low, it is the only region dominated by peatland fires (PEAT), with PEAT emissions contributing as much as 91.34 Tg yr^{-1} of CO_2 (48.4% of the regional total). This uniqueness stems from its specific fire regime: vast areas of organic-rich peatlands become highly flammable after being drained and converted to agricultural land (e.g., oil palm plantations). Such fires often manifest as long-duration, hard-to-extinguish subsurface smoldering, leading to extremely high carbon emission intensities and making EQAS a unique and closely watched case in global biomass burning research.

The spatial heterogeneity of this uncertainty is illustrated in Figs. 2b and 2c, which map the highest and lowest emission estimates across the ensemble. Globally, the uncertainty is substantial, with the maximum estimate of annual CO_2 emissions being 2.2 times higher than the minimum estimate across the MBEI sub-inventories.

Importantly, high biomass burning emission uncertainty is not found in traditional biomass burning hotspots. Instead, some of the highest uncertainties are found in regions with lower overall emissions. Specifically, Australia and New Zealand (AUST) and the Middle East (MIDE) exhibit the greatest uncertainty, with maximum-to-minimum (max/min) emission ratios reaching 7.18 and 6.40, respectively. In AUST, this extreme uncertainty is linked to its fire regime dominated by highly intermittent and catastrophic megafires (e.g., the 2019–2020 events), which pose significant challenges to consistent estimation across different algorithms. In MIDE, which contributes only 0.52% to the global total, the high uncertainty stems from small, scattered AGRI and SAVA. These weak fire signals are near the lower limit of satellite detection capabilities, a fact confirmed by the large discrepancy observed when comparing estimates derived from 'all confidence' versus 'high and medium confidence' active fire data. In contrast, the major tropical burning regions show much lower relative uncertainty, despite their massive contribution to global emissions. The African (SHAF, NHAF) and South American (SHSA) hotspots have max/min ratios consistently below 2.0. This greater consensus among methods is attributable to the nature of their fires: large-scale, intense, and seasonally predictable SAVA that are robustly captured by various estimation approaches. Meanwhile, temperate and high-latitude regions

such as Central Asia (CEAS), BONA, and Europe (EURO) show intermediate levels of uncertainty, with max/min ratios between 3.5 and 4.0.

In summary, this analysis reveals a critical divergence between the spatial patterns of emission magnitudes and their estimation uncertainties. While emission hotspots are concentrated in tropical regions dominated by regular SAVA and DEFO, the highest uncertainties occur in areas characterized by either highly intermittent megafires (e.g., AUST) or weak, scattered burning (e.g., MIDE), posing distinct challenges to current estimation methods.

Table 3. Total annual CO_2 emissions (Maximum, Minimum, and Average, unit: Tg) for 2003–2023.

Year	Maximum	Minimum	Average	Year	Maximum	Minimum	Average
2003	10882.90	4487.65	7673.68	2014	9258.62	4489.87	7265.29
2004	10842.08	4271.50	7522.16	2015	9688.74	5035.46	7701.46
2005	10391.58	4350.62	7328.15	2016	8476.61	4059.68	6789.30
2006	9663.37	4160.83	7077.83	2017	9250.64	4436.15	7042.77
2007	11063.35	4641.22	7751.48	2018	8727.34	4160.93	6911.22
2008	9725.05	4030.68	6925.95	2019	9747.60	4971.22	7657.46
2009	8661.02	3930.36	6669.83	2020	9295.62	4375.98	7249.50
2010	10253.23	4748.50	7554.59	2021	10696.69	4767.44	7705.11
2011	9653.73	4119.74	7205.26	2022	7289.55	3348.45	6442.83
2012	10537.30	4721.32	7895.63	2023	10527.88	5206.72	8506.96
2013	8161.82	4087.36	6489.87	Mean	9656.89	4400.08	7303.16

3.2 Seasonality of biomass burning emissions

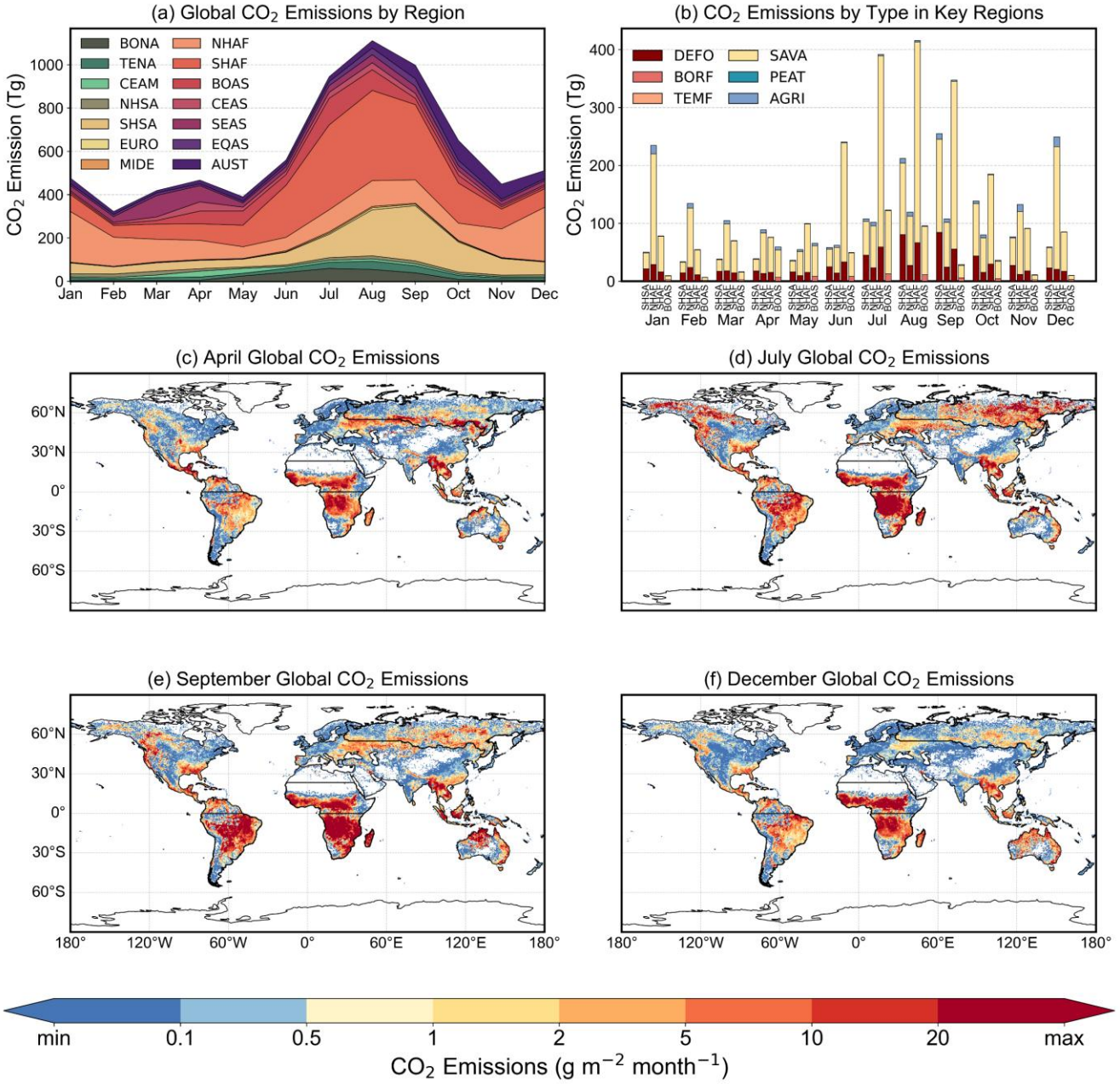

Figure 3. Seasonal cycle and spatial dynamics of global biomass burning CO_2 emissions (mean of 2003–2023). (a) Global monthly emissions partitioned by source region. (b) Monthly emissions for the four primary contributing regions, showing the composition by fire type. (c-f) Spatial distribution of mean monthly emission flux during key seasonal phases: April, July, September, and December.

The MBEI 2003–2023 CO_2 emission inventory reveals a distinct bimodal seasonal cycle (Fig. 3a). Global emissions reach a minimum in February and then climb to a primary peak in the Northern Hemisphere's late summer (August–September). This global pattern results from the combined effect of staggered fire seasons in key regions. Four regions in particular (SHAF, NHAF, SHSA, and BOAS) drive this cycle,

collectively accounting for over 71% of total annual emissions (Fig. 3b). For a detailed view of the emission sources, Fig. S7 shows the monthly composition of CO_2 emissions by the six fire types for each of the 14 global regions during 2003–2023.

The annual cycle begins its ascent after the global minimum in February, initially driven by fire activity in the Northern Hemisphere. Persistent dry-season burning in NHAF transitions into an intensifying fire season across Eurasia. By April, the focus of burning activity clearly shifts northward, with emissions surging in regions like BOAS, while the major Southern Hemisphere burning regions (SHAF and SHSA) remain in a period of low activity (Fig. 3c).

From May onwards, global emissions accelerate rapidly, driven by the increasing overlap of fire seasons in both hemispheres. While boreal fires in regions like BOAS reach their annual peak in July, the dominant driver of this global surge is the explosive onset of the fire season in SHAF. Concurrently, burning intensifies in SHSA, and this synergistic effect pushes global emissions towards their annual maximum (Fig. 3d).

The global emission peak in August and September is dominated by the Southern Hemisphere, as fire activity wanes in the major Northern Hemisphere regions. During this period, burning in SHSA reaches its annual zenith, fueled by a combination of DEFO and SAVA. Although past its own peak, SHAF remains the single largest regional contributor to global emissions (Fig. 3e).

Beginning in October, the onset of the rainy season in the Southern Hemisphere rapidly suppresses fire activity there, causing a sharp decline in global emissions. This marks a decisive shift in the global burning pattern. The focus of activity returns entirely to NHAF, which enters its primary fire season that lasts through the subsequent winter (Fig. 3f). This distinct hemispheric seesaw effect completes the annual cycle. Fig. S8 presents the spatial distribution patterns of monthly CO_2 emissions from global biomass burning during the period 2003–2023.

3.3 Interannual variability and long-term trends

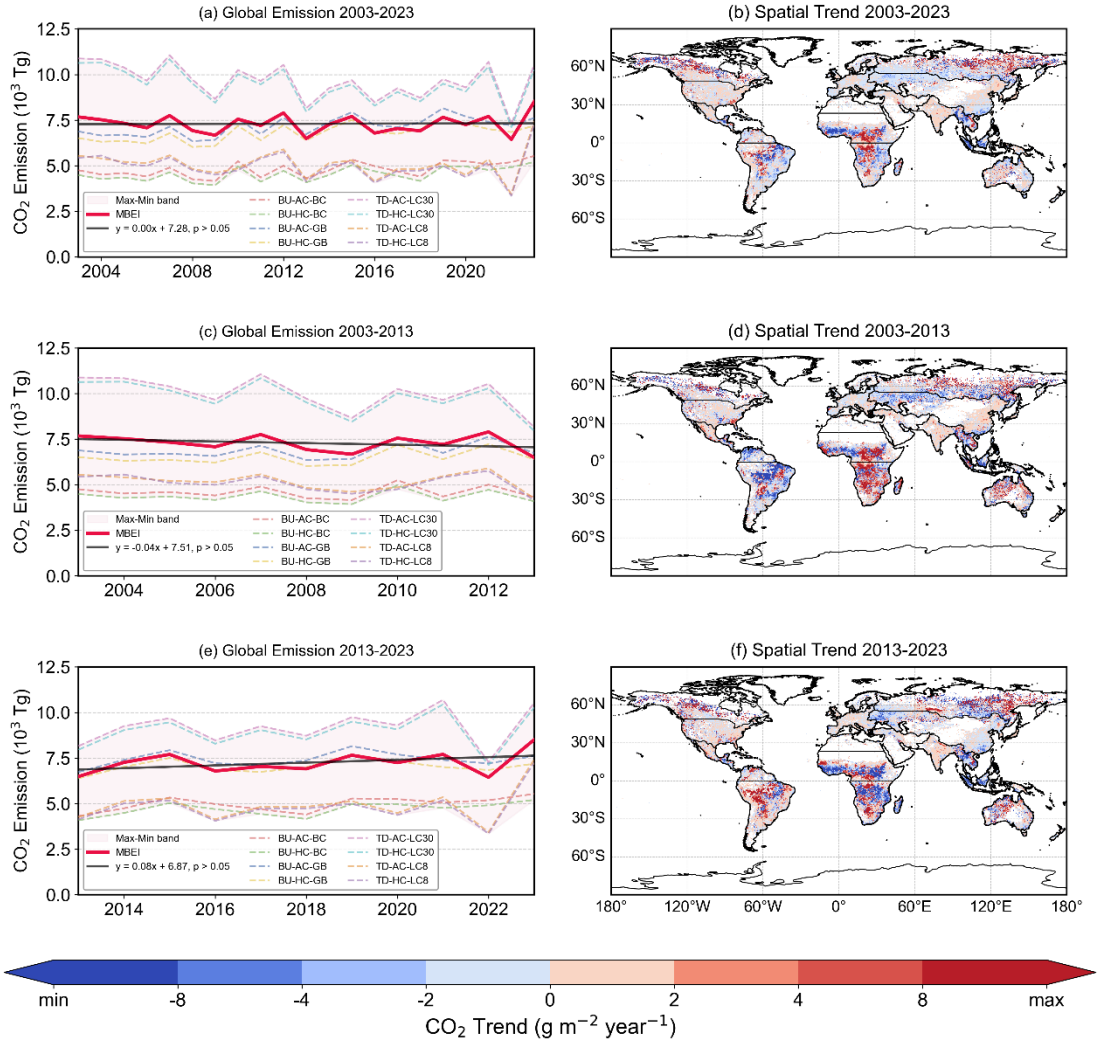

Figure 4. Temporal and spatial trends of global biomass burning CO_2 emissions from 2003 to 2023. (a, c, e) Interannual variation of total emissions and (b, d, f) trends in emission flux for three periods: 2003–2023, 2003–2013, and 2013–2023.

Over the 2003–2023 study period, global biomass burning CO_2 emissions are characterized not by a significant long-term trend but by pronounced interannual variability. Specifically, the time series of global annual CO_2 emissions, derived from the MBEI, which integrates eight sub-inventories, shows no statistically significant long-term trend ($p > 0.05$; Fig. 4a). This pattern of high interannual variability, coupled with a lack of a significant long-term trend, is also observed for other major emitted species (Fig. S9). This strong interannual variability is a well-documented feature of global fire activity, primarily linked to climate anomalies such as the El Niño-Southern Oscillation (ENSO) (Chen et al., 2017; Mariani et al., 2016 ; Li et al., 2023). Our time-series analysis confirms this link: emission peaks (e.g., 2010, 2015,

2019) consistently coincide with major El Niño events that trigger widespread drought, while emission troughs (e.g., 2009, 2022) align with wetter La Niña conditions. The sharp contrast between the low emissions during the 2022 La Niña and the subsequent spike during the 2023 El Niño starkly illustrates the powerful influence of the ENSO cycle on global fire activity.

Alongside these climate-driven variations, the MBEI is characterized by a broad uncertainty range, stemming from differences in algorithm structures and input data. The spread between MBEI estimates (the Max-Min band in Figs. 4a, c, e) is considerable, with the difference between the highest and lowest annual totals exceeding 2600 Tg in some years (e.g., 2004, 2022). This divergence arises from methodological differences, particularly between top-down (FRP-based) and bottom-up (burned area-based) approaches in areas like fire detection and combustion parameterization. Critically, however, despite the large spread in absolute emission values, the MBEI sub-inventories show strong agreement on the relative interannual patterns, consistently identifying the same peak and trough years.

This apparent global stability masks significant and opposing regional trends, producing a highly heterogeneous spatial pattern of change (Fig. 4b). Over the full 21-year period, statistically significant trends were concentrated in Asia. BOAS exhibited a strong and significant increasing trend in emission flux at a rate of 15.71 g m^{-2} yr^{-1} ($p < 0.01$). In contrast, CEAS and SEAS showed significant decreasing trends of -1.72 g m^{-2} yr^{-1} ($p < 0.01$) and -2.08 g m^{-2} yr^{-1} ($p < 0.05$), respectively (Table S6). Fig. 4b suggests decreases in equatorial Africa and central-southern South America, and increases in BONA, these trends were not statistically significant when aggregated over the entire 14 GFED regions for the 2003–2023 period. This highlights an offsetting pattern, where declining emissions in some regions are partially balanced by increases elsewhere, contributing to the lack of a significant global trend.

A decadal comparison between 2003–2013 and 2013–2023 reveals substantial evolution in these spatial patterns, indicating a major shift in the global distribution of biomass burning emissions (Figs. 4d, f).

During the first decade (2003–2013), a slight but statistically non-significant global decrease ($p > 0.05$; Fig. 4c) masked a profound spatial redistribution of fire activity. The dominant feature was a significant increase in fire emissions in SHAF, which saw an upward trend of 4.41 g m^{-2} yr^{-1} ($p < 0.05$). By contrast, South America experienced significant decreases, particularly in NHSA where emissions declined at a rate of -4.97 g m^{-2} yr^{-1} ($p < 0.05$). Simultaneously, a strong decreasing trend was observed in CEAS, with a rate of -2.96 g m^{-2} yr^{-1} ($p < 0.05$). Boreal regions and Southeast Asia showed no statistically significant regional trends during this period (Fig. 4d and Table S7).

In the subsequent decade (2013–2023), this pattern shifted markedly. Although the global emission trajectory did not exhibit a statistically significant linear trend ($p > 0.05$), it transitioned from a slight decline to an overall increase (Fig. 4e), signaling a clear decadal change in biomass burning dynamics. This shift is more appropriately characterized as a structural transformation rather than a linear progression, driven by a marked increase in both the frequency and intensity of extreme emission years (e.g., 2015, 2019, 2023). The 2015–2016 ENSO cycle exemplifies this mechanism, as the super El Niño event in 2015 induced catastrophic PEAT in Indonesia (EQAS) and elevated global emissions to a record peak, which was subsequently followed by a pronounced decline in 2016 with the onset of a strong La Niña (Whitburn et al., 2016; Yin et al., 2020a). The 2023 fire season was even more pronounced, as an unprecedented wildfire season in boreal Canada (BONA) coincided with a developing El Niño, jointly driving global annual emissions to the highest level in our 21-year record. Detailed regional statistics, including the annual mean CO_2 emission fluxes and their corresponding Theil-Sen slope trends across the 14 study regions for the 2013–2023 period, are summarized in Table S8 (Jain et al., 2024; Luo et al., 2025).

Spatially, this decadal shift is characterized by a reversal of trends in Africa and South America (Fig. 4f). Africa, which previously showed increasing trends in the south, now exhibited a pronounced and significant decrease in NHAF, with emissions declining at -5.14 g m^{-2} yr^{-1} ($p < 0.05$). In a direct reversal of the previous decade, SHSA showed a strong and significant increase of 8.01 g m^{-2} yr^{-1} ($p < 0.01$). Notably, despite the visually striking increases in BONA and northern Eurasia driven by the extreme fire years mentioned previously, the linear trends for these aggregated regions over the 2013–2023 period were not statistically significant, suggesting that the changes were dominated by episodic events rather than a consistent year-over-year increase.

In summary, beneath the overall stable trend of global biomass burning emissions over the past 21 years, there lies a key decadal shift, from a declining phase dominated by weakening fire activity in the tropics (2003–2013) to an increasing phase driven by intensifying fire activity in high-latitude regions and parts of the Southern Hemisphere (2013–2023).

3.4 Inter-comparison with other inventories

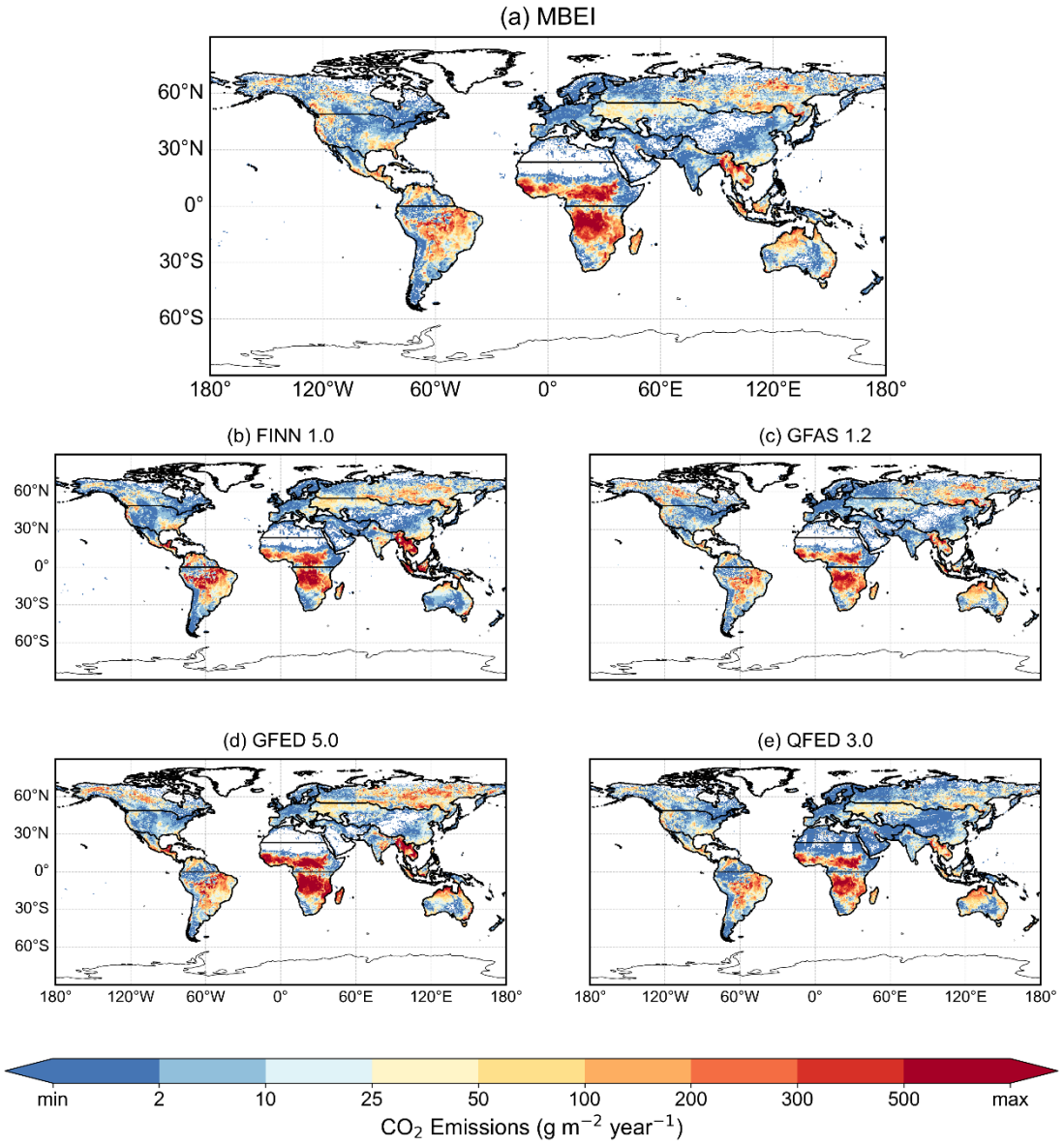

Figure 5. Comparison of multi-year mean spatial patterns of global CO_2 emissions estimated by different biomass burning inventories (2003–2022). (a) The mean of the eight inventories constructed in this study. (b) Fire INventory from NCAR version 2.5 (FINN 2.5), (c) Global Fire Assimilation System version 1.2 (GFAS 1.2), (d) Global Fire Emissions Database version 5.0 (GFED 5.0), and (e) Quick Fire Emissions Dataset version 3.1 (QFED 3.1).

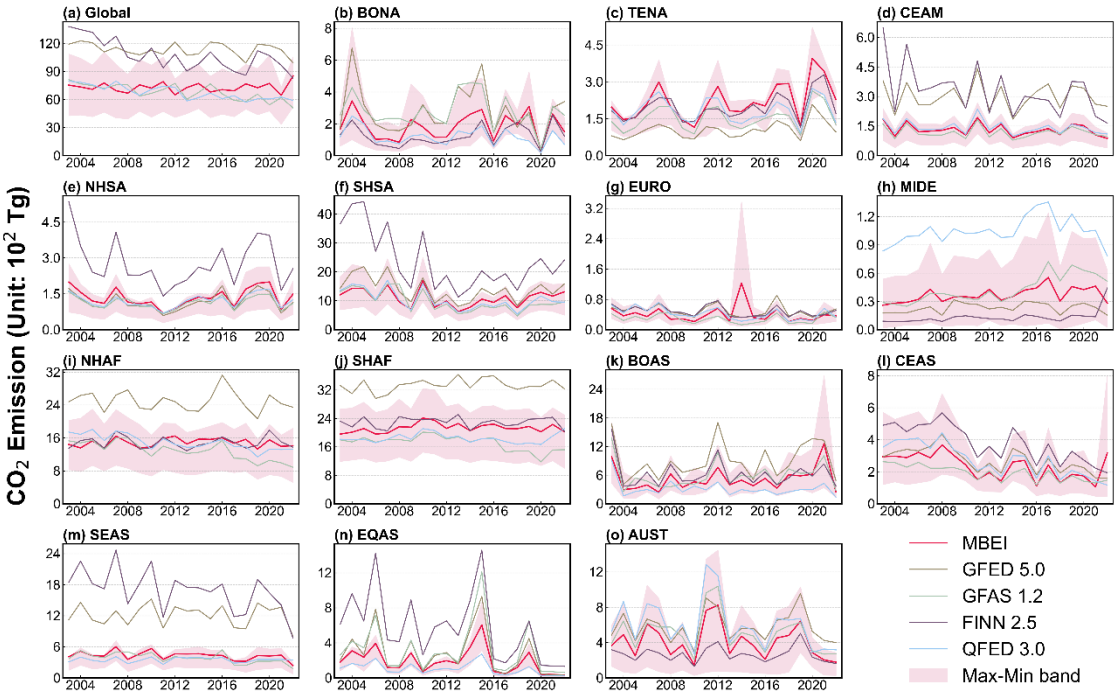

Figure 6. Time series of interannual variability in biomass burning CO_2 emissions from different inventories at global and regional scales (2003–2022). (a) Total annual global CO_2 emissions from this study's inventory and four other inventories. (b) to (o) Total annual CO_2 emissions from this study's inventory and four other inventories across 14 regions.

A comparison of biomass burning CO_2 emissions reveals broad spatial agreement across all inventories (including the MBEI from this study, FINN 2.5, GFAS 1.2, GFED 5.0, and QFED 3.1) (Fig. 5). Furthermore, the emission magnitudes from these inventories are largely consistent, with no significant discrepancies. In addition, comparative analyses are performed for three emission species, namely SO_2, $PM_{2.5}$ and BC and the results are presented in Figs. S10–S15 in the Supplementary Material. These species represent different components and combustion phases of biomass burning. SO_2 reflects the combustion of naturally occurring sulfur-containing organic matter and inorganic sulfides in biomass, $PM_{2.5}$ represents the overall intensity of total particulate matter emissions, and BC indicates incomplete combustion during the high-temperature flaming phase. Similar to CO_2, the spatial patterns for these species are largely consistent across inventories. While the products capture similar interannual variability, their estimates of emission magnitudes reveal substantial inter-inventory uncertainty (results show in Figs. S10–S15). All products successfully identify the primary global fire hotspots, including those in Africa (SHAF, NHAF), South America (SHSA), Southeast Asia (SEAS), and the northern boreal forests (BONA, BOAS).

However, significant discrepancies exist in both emission magnitude and spatial detail among various inventories (Fig. 6). The uncertainty range (Max-Min band) of the MBEI generally encompasses the estimates from all reference products across most regions, suggesting that it effectively captures the structural uncertainty among inventories. Moreover, the mean estimate of the MBEI typically resides near the center of the various inventories. With respect to magnitude and trend, our inventory exhibits the closest alignment with GFAS. GFED consistently provides the highest global estimates, while FINN ranks second and in some regions even exceeds GFED, whereas QFED remains generally lower. Despite these differences in magnitude, all inventories demonstrate strong consistency in interannual variability, successfully capturing major global fire years (e.g., 2010, 2015, 2019).

A regional analysis highlights significant divergences among emission inventories, particularly in the high-emission tropics where the MBEI's uncertainty band is often substantial. In the African savannas (NHAF, SHAF), the MBEI mean estimate is consistently lower than GFED 5.0, often residing in the lower half of the inter-inventory range (Figs. 6i, j). For instance, in SHAF, GFED 5.0 estimates are frequently approximately 10 Tg yr^{-1} higher than the MBEI mean, while our estimate aligns closely with GFAS 1.2 and QFED 3.0. Conversely, in regions with significant DEFO and AGRI fires like SHSA and SEAS, FINN 2.5 estimates consistently occupy the upper portion of the inter-inventory range. In these areas, the MBEI mean is again more conservative, and our Max-Min band effectively captures the cluster of lower estimates from GFED, GFAS, and QFED (Figs. 6f, m).

In contrast, inter-inventory agreement is generally higher in low- to moderate-emission regions at mid- to high latitudes, where the MBEI mean closely tracks the multi-inventory average (e.g., Temperate North American (TENA) and EURO; Figs. 6c, 6g). However, this consistency breaks down in boreal forests during years with episodic, large-scale fires. In these instances, the value of the Max-Min band becomes particularly evident. During the extreme BONA fire year of 2004, estimates spanned a wide range from FINN 2.5 (2.2 Tg) to GFED 5.0 (6.7 Tg). Critically, our own Max-Min band for that year expanded dramatically (from 1.0 to 8.0 Tg), explicitly quantifying the immense challenge and uncertainty in capturing such events. A similar expansion of our uncertainty band is observed in BOAS during its severe 2021 fire season, where our maximum estimate reached 26.8 Tg, encompassing the high values from other inventories.

Regions dominated by specific fuel types, such as the peatlands of EQAS, reveal fundamental methodological differences that are well-framed by our uncertainty analysis. While all inventories

583 captured the 2015 El Niño-driven fire peak, the estimated magnitude varied by more than five-fold, from
584 QFED 3.0 (2.7 Tg) to FINN 2.5 (14.6 Tg) (Fig. 6n). The MBEI mean estimate (6.0 Tg) and its associated
585 uncertainty band (3.2–8.6 Tg) are positioned centrally among these estimates, with its upper bound
586 approaching the GFED 5.0 value (9.3 Tg) while excluding the extreme high and low outliers. This
587 indicates that, under substantial uncertainty in quantifying PEAT emissions, the MBEI delineates a
588 comprehensive Max–Min band and provides a stable central mean estimate within it.
589 In summary, our comparison demonstrates that while existing inventories agree on broad spatiotemporal
590 patterns, significant quantitative disagreements persist, particularly in tropical regions and during
591 extreme fire events. Against this backdrop, the MBEI provides a new, synthesized central estimate and a
592 robust uncertainty range (Max-Min band). Its central estimate is consistent with the ensemble median,
593 and its uncertainty bounds effectively encompass the spread across different inventories. This central
594 estimate and a quantified uncertainty range not only offers a reliable measure of biomass burning
595 emissions but also serves as a diagnostic tool, highlighting the specific regions (e.g., African savannas,
596 Southeast Asian peatlands) and conditions (e.g., extreme boreal fires) that drive the largest inter-
597 inventory discrepancies, thereby providing a clear basis for future inventory refinement.

598 **4 Discussion**

599 **4.1 Advancement and uncertainty assessment**

600 This study introduces the MBEI, a systematic emission estimation framework built upon a framework of
601 eight sub-inventories, integrating both bottom-up and top-down approaches with various combinations
602 of key input data. The emission range of the MBEI provides a direct measure of structural uncertainty,
603 allowing modelers to assess the sensitivity of their simulations to inventory choice (high-end vs. low-
604 end estimates). This addresses a long-standing challenge in climate and atmospheric chemistry modeling,
605 where discrepancies among emission inventories are a recognized major source of the simulation
606 uncertainty (Pan et al., 2020; Su et al., 2023). The MBEI framework systematically quantifies this
607 uncertainty, revealing two key findings. First, the uncertainty is substantial in magnitude, with the
608 maximum global annual CO_2 estimate across the sub-inventories being 2.2 times the minimum. Second,
609 and perhaps more importantly, the uncertainty exhibits significant spatial heterogeneity, with the highest

relative uncertainty not coinciding with traditional emission hotspots, but instead found in regions with lower emissions, such as AUST and MIDE.

This divergence is strongly linked to how regional land cover and fire regime characteristics amplify the sensitivity of different estimation methodologies. For instance, in AUST, the fire regime is dominated by event-driven, extremely high-intensity megafires. These events pose significant challenges for both FRP-based algorithms, which can be prone to saturation, and burned area-based methods, which struggle to accurately map such intense and rapidly spreading fires. Conversely, in the MIDE, the high uncertainty arises from weak, small-scale, and scattered AGRI or SAVA. These fires are often near the detection limits of satellite sensors, causing emission estimates to be highly sensitive to the chosen active fire detection confidence thresholds. In stark contrast, African savannas, despite their high emission fluxes, show lower relative uncertainty. Their widespread and seasonally predictable fires are robustly captured by both top-down and bottom-up approaches, leading to greater convergence among the different methods. This finding implies that future efforts to refine emission inventories should extend beyond traditional hotspots to better understand and parameterize the distinct combustion processes in these atypical fire regimes.

The MBEI's 21-year analysis also uncovers a critical shift in the long-term dynamics of global emissions. Despite a stable trend overall, we identify a clear decadal transition: from a slight decline dominated by weakening tropical fires (2003–2013) to a rising phase driven by intensifying boreal fires and more frequent extreme events (2013–2023). This dynamic, characterized by a decline in tropical fire activity and an increase in boreal fire activity, synthesizes seemingly disparate observations, such as the global decrease in burned area (Andela et al., 2017) and the lengthening of fire seasons in high-latitude regions (Jones et al., 2022), into a coherent narrative at the emission level. Particularly in the second decade, climate-driven extreme events, such as the 2015 Indonesian peat fires, the 2019–2020 Australian megafires, and the 2023 Canadian wildfires, significantly reshaped the global emission record. This underscores the growing influence of climate change on global biomass burning emissions, a shift with profound implications for the global carbon cycle and its associated climate feedbacks.

4.2 Limitations and Future Perspectives of the MBEI Framework

The MBEI framework aims to quantify the structural uncertainty in global biomass burning emissions by ensembling multiple algorithmic approaches. However, the accuracy of any emission inventory is inherently constrained by the spatiotemporal resolution and physical sensitivity of its input data. The

uncertainty ranges revealed in this study, which span various regions and biomes, largely reflect the physical limitations of current Earth observation systems in capturing extreme fire behaviors and complex surface processes, alongside the methodological differences discussed.

A key decision in this study was to use MODIS active fire products (MCD14DL) exclusively for the 2003–2023 period. Although the Visible Infrared Imaging Radiometer Suite (VIIRS), available since 2012, offers superior spatial resolution (375 m) compared to MODIS (1 km), applying it would have limited the consistent time series to the post-2012 era. Merging MODIS (2003–2011) and VIIRS (2012–2023) records introduces a risk of inconsistency; the higher detection sensitivity of VIIRS could result in an artificial increase in fire counts, which might be misinterpreted as a real upward trend in global fire activity. To maintain the homogeneity of the 21-year dataset for trend analysis, we prioritized sensor consistency. We acknowledge that this choice likely leads to an underestimation of emissions from small-scale agricultural fires, particularly in regions like the Middle East or India, where fires are often smaller than the MODIS detection threshold (Hantson et al., 2013; Justice et al., 2002; Vadrevu and Lasko, 2018).

In addition to sensor specifications, most current inventories relying on optical remote sensing face inherent physical limits driven by environmental heterogeneity. Complex surface conditions can constrain the effectiveness of estimation methods. For instance, in the peatlands of Equatorial Asia (e.g., Indonesia), fires often occur as subsurface low-temperature smoldering. The thermal radiation from these fires is frequently too weak to trigger standard satellite detection algorithms (Rein and Huang, 2021; Sofan et al., 2019). Similarly, in dense tropical rainforests, the canopy layer can occlude or absorb thermal radiation emitted by understory fires (East et al., 2023). These scenarios contribute to omission errors in top-down, FRP-based approaches (Morton et al., 2013; Tyukavina et al., 2022). Conversely, while bottom-up methods based on burned area can capture the spatial traces of these fires, they face challenges in accurately determining the depth of burn in organic soils (Ballhorn et al., 2009; Wiggins et al., 2018). Therefore, despite the integration of multiple algorithms in MBEI, these physical constraints suggest a potential underestimation in our emission estimates for these specific biomes.

Looking forward, the flexible architecture of MBEI is designed to incorporate emerging datasets to address these limitations. As the observational record of VIIRS extends, future versions of MBEI will integrate these data to improve the detection of small-scale fires once a sufficiently long and consistent record is established. Furthermore, data from new-generation geostationary satellites (e.g., FY-4, Himawari-8/9, GOES-R) offer a significant improvement in temporal resolution. Minute-level

observations from these platforms will enable the direct integration of the Fire Radiative Power diurnal cycle, reducing the reliance on Gaussian extrapolation from sparse polar-orbiter snapshots and enhancing the physical realism of Fire Radiative Energy estimation.

Advancements in next-generation satellites will also enhance the MBEI's capacity for fuel load estimation. In this study, due to the lack of high-resolution annual AGB observations, we adjusted static AGB maps using interannual variations in NPP. However, AGB is a cumulative stock variable, whereas NPP is an annual flux variable. Their relationship is complex and influenced by factors such as lag effects, tree mortality, and decomposition, meaning a high NPP year does not always result in an immediate biomass increase (Keeling and Phillips, 2007; Teets et al., 2022). Future versions of MBEI aim to improve this by integrating dynamic AGB datasets from active remote sensing missions. Specifically, spaceborne LiDAR (e.g., NASA GEDI) and P-band SAR (e.g., ESA BIOMASS mission) are expected to provide global measurements of forest vertical structure. This will allow MBEI to incorporate dynamic fuel loads, thereby reducing a major source of uncertainty in the bottom-up approach based on burned area (Cao et al., 2016; Liu et al., 2019; Rodríguez-Fernández et al., 2018).

Finally, current emission estimates rely on static EFs, which may not fully capture the variability of combustion efficiency within biomes or during a fire's lifecycle (van Leeuwen et al., 2013; Yin, 2022). Future improvements are expected to come from developing comprehensive EF databases through advanced molecular-level aerosol speciation (Jen et al., 2019; Koss et al., 2018). Complementing this, dynamic high-resolution EF datasets could be generated using synchronous satellite trace gas retrievals. For example, the ratio of carbon monoxide to nitrogen dioxide (ΔNO_2 / ΔCO) columns derived from the TROPOMI sensor can serve as a near-real-time proxy for combustion efficiency (flaming vs. smoldering) (van der Velde et al., 2021). By assimilating such dynamic proxies, MBEI aims to evolve toward a more dynamic monitoring system.

In conclusion, while the current version of MBEI quantifies uncertainty by integrating established methods, its modular design serves as a platform for incorporating new data inputs as they become available. This ensures a feasible pathway for iterative refinement, supporting more comprehensive assessments of global biomass burning emissions.

5 Conclusion

This study systematically assessed global biomass burning emissions and their uncertainties from 2003–2023 using the MBEI, an ensemble framework of eight sub-inventories that integrates both bottom-up and top-down approaches. A key finding is the spatial separation between the emission hotspots and the uncertainty hotspots. While high-emission regions in Africa and South America account for 64.4% of global CO_2 emissions, the structural uncertainty there is relatively constrained (max/min ratio < 2.0). In contrast, the greatest uncertainty (max/min ratio > 6.0) is found in lower-emission regions characterized by extreme, intermittent fires (e.g., AUST) or scattered agricultural burning (e.g., the MIDE).

Temporally, our analysis reveals a significant shift in the drivers of global biomass burning emissions over the past two decades. Although the overall long-term trend is not statistically significant, we identify a clear transition: the period dominated by declining tropical fire activity (2003–2013) was followed by a period increasingly influenced by intensifying high-latitude boreal fires and frequent climate-driven extreme events (2013–2023).

The spatial heterogeneity and temporal shift highlight the growing complexity of the global biomass burning emission regimes. The primary contribution of the MBEI framework is therefore its ability to explicitly quantify this structural uncertainty. It provides a central estimate consistent with the multi-inventory average, along with an uncertainty range that encompasses the estimates of major existing products. MBEI offers the crucial boundary conditions needed for Earth system models to estimate related environmental or exposure risk.

To effectively assess the complex dynamics of global biomass burning emission, the results of this study indicate that the focus should evolve from pursuing a single best estimate to embracing a probabilistic, uncertainty-aware approach. It is suggested that such data-constrained uncertainty information should be directly integrated into atmospheric chemistry and Earth system models. This is essential not only for improving model fidelity but also for conducting more robust risk assessments that consider plausible high-end emission scenarios. Ultimately, the MBEI's explicit quantification of uncertainty provides a more solid scientific foundation for developing resilient environmental and climate policies.

Data availability. The developed MBEI emission inventory described in this paper is available from Zenodo: 10.5281/zenodo.18104830 (Liu and Yin, 2025). For further support or guidance regarding data use, please contact yinshuai@aircas.ac.cn.

Supplement.

Author contributions. SY and ZS were responsible for the conceptualization of the study, project administration, supervision, and funding acquisition. XL designed the methodology, developed the software, performed the formal analysis and investigation, curated the data, prepared the visualizations and wrote the original draft of the manuscript. CS contributed to the methodology development and software implementation. TN, PW, QC and LS assisted with the formal analysis and data curation. HS, DJ, MG, KY, ZT, LW, and XL contributed to the investigation, validation, and provision of resources. All authors participated in the review and editing of the manuscript and have approved the final version for publication.

Competing interests. The contact author has declared that none of the authors has any competing interests.

Disclaimer. Publisher's note: Copernicus Publications remains neutral with regard to jurisdictional claims in published maps and institutional affiliations. While Copernicus Publications makes every effort to ensure appropriate place names are included, the final responsibility lies with the authors.

Acknowledgements. The authors would like to thank J. W. Kaiser for providing access to the most recent data. We also acknowledge the support of the State Key Laboratory of Remote Sensing and Digital Earth, Aerospace Information Research Institute, Chinese Academy of Sciences. The authors extend their gratitude to the anonymous reviewers for their constructive comments, which greatly helped improve the quality of this paper.

Financial support. This research is supported by the National Natural Science Foundation of China (grant no. 42475142).

Reference

Andela, N., Kaiser, J. W., van der Werf, G. R., and Wooster, M. J.: New fire diurnal cycle characterizations to improve fire radiative energy assessments made from MODIS observations, Atmospheric Chemistry and Physics, 15, 8831–8846, https://doi.org/10.5194/acp-15-8831-2015, 2015.

Andela, N., Morton, D. C., Giglio, L., Chen, Y., van der Werf, G. R., Kasibhatla, P. S., DeFries, R. S., Collatz, G. J., Hantson, S., Kloster, S., Bachelet, D., Forrest, M., Lasslop, G., Li, F., Mangeon, S., Melton, J. R., Yue, C., and Randerson, J. T.: A human-driven decline in global burned area, Science, 356, 1356–1362, https://doi.org/10.1126/science.aal4108, 2017.

Andreae, M. O. and Merlet, P.: Emission of trace gases and aerosols from biomass burning, Global Biogeochemical Cycles, 15, 955–966, https://doi.org/10.1029/2000GB001382, 2001.

Andreae, M. O.: Emission of trace gases and aerosols from biomass burning – an updated assessment, Atmospheric Chemistry and Physics, 19, 8523–8546, https://doi.org/10.5194/acp-19-8523-2019, 2019.

Ballhorn, U., Siegert, F., Mason, M., and Limin, S.: Derivation of burn scar depths and estimation of carbon emissions with LIDAR in Indonesian peatlands, Proceedings of the National Academy of Sciences, 106, 21213–21218, https://doi.org/10.1073/pnas.0906457106, 2009.

Binte Shahid, S., Lacey, F. G., Wiedinmyer, C., Yokelson, R. J., and Barsanti, K. C.: NEIVAv1.0: Next-generation emissions inventory expansion of Akagi et al. (2011) version 1.0, Geoscientific Model Development, 17, 7679–7711, https://doi.org/10.5194/gmd-17-7679-2024, 2024.

Bowman, D. M. J. S., Balch, J. K., Artaxo, P., Bond, W. J., Carlson, J. M., Cochrane, M. A., D'Antonio, C. M., DeFries, R. S., Doyle, J. C., Harrison, S. P., Johnston, F. H., Keeley, J. E., Krawchuk, M. A., Kull, C. A., Marston, J. B., Moritz, M. A., Prentice, I. C., Roos, C. I., Scott, A. C., Swetnam, T. W., van der Werf, G. R., and Pyne, S. J.: Fire in the earth system, Science, 324, 481–484, https://doi.org/10.1126/science.1163886, 2009.

Bowman, D. M. J. S., Kolden, C. A., Abatzoglou, J. T., Johnston, F. H., van der Werf, G. R., and Flannigan, M.: Vegetation fires in the Anthropocene, Nature Reviews Earth & Environment, 1, 500–515, https://doi.org/10.1038/s43017-020-0085-3, 2020.

Bray, C. D., Battye, W. H., Aneja, V. P., and Schlesinger, W. H.: Global emissions of NH_3, NO_x, and N_2O from biomass burning and the impact of climate change, Journal of the Air & Waste Management Association, 71, 102–114, https://doi.org/10.1080/10962247.2020.1842822, 2021.

Cao, L., Coops, N. C., Innes, J. L., Sheppard, S. R. J., Fu, L., Ruan, H., and She, G.: Estimation of forest biomass dynamics in subtropical forests using multi-temporal airborne LiDAR data, Remote Sensing of Environment, 178, 158–171, https://doi.org/10.1016/j.rse.2016.03.012, 2016.

780 Chen, Y., Morton, D. C., Andela, N., van der Werf, G. R., Giglio, L., and Randerson, J. T.: A pan-tropical
781 cascade of fire driven by el niño/southern oscillation, Nature Climate Change, 7, 906–911,
782 https://doi.org/10.1038/s41558-017-0014-8, 2017.
783 Cunningham, C. X., Williamson, G. J., and Bowman, D. M. J. S.: Increasing frequency and intensity of
784 the most extreme wildfires on earth, Nature Ecology & Evolution, 8, 1420–1425,
785 https://doi.org/10.1038/s41559-024-02452-2, 2024.
786 Filonchyk, M., Peterson, M. P., Zhang, L., Hurynovich, V., and He, Y.: Greenhouse gases emissions and
787 global climate change: Examining the influence of CO_2, CH_4, and N_2O, Science of The Total
788 Environment, 935, 173359, https://doi.org/10.1016/j.scitotenv.2024.173359, 2024.
789 Friedl, M. and Sulla-Menashe, D.: MODIS/terra+aqua land cover type yearly L3 global 500m SIN grid
790 V061, NASA LP DAAC [data set], https://doi.org/10.5067/MODIS/MCD12Q1.061, 2022.
791 East, A., Hansen, A., Armenteras, D., Jantz, P., and Roberts, D. W.: Measuring understory fire effects
792 from space: Canopy change in response to tropical understory fire and what this means for applications
793 of GEDI to tropical forest fire, Remote Sensing, 15, 696, https://doi.org/10.3390/rs15030696, 2023.
794 Friedlingstein, P., O'Sullivan, M., Jones, M. W., Andrew, R. M., Hauck, J., Landschützer, P., Le Quéré,
795 C., Li, H., Luijkx, I. T., Olsen, A., Peters, G. P., Peters, W., Pongratz, J., Schwingshackl, C., Sitch, S.,
796 Canadell, J. G., Ciais, P., Jackson, R. B., Alin, S. R., Arneth, A., Arora, V., Bates, N. R., Becker, M.,
797 Bellouin, N., Berghoff, C. F., Bittig, H. C., Bopp, L., Cadule, P., Campbell, K., Chamberlain, M. A.,
798 Chandra, N., Chevallier, F., Chini, L. P., Colligan, T., Decayeux, J., Djeutchouang, L. M., Dou, X., Duran
799 Rojas, C., Enyo, K., Evans, W., Fay, A. R., Feely, R. A., Ford, D. J., Foster, A., Gasser, T., Gehlen, M.,
800 Gkritzalis, T., Grassi, G., Gregor, L., Gruber, N., Gürses, Ö., Harris, I., Hefner, M., Heinke, J., Hurtt, G.
801 C., Iida, Y., Ilyina, T., Jacobson, A. R., Jain, A. K., Jarníková, T., Jersild, A., Jiang, F., Jin, Z., Kato, E.,
802 Keeling, R. F., Klein Goldewijk, K., Knauer, J., Korsbakken, J. I., Lan, X., Lauvset, S. K., Lefèvre, N.,
803 Liu, Z., Liu, J., Ma, L., Maksyutov, S., Marland, G., Mayot, N., McGuire, P. C., Metzl, N., Monacci, N.
804 M., Morgan, E. J., Nakaoka, S.-I., Neill, C., Niwa, Y., Nützel, T., Olivier, L., Ono, T., Palmer, P. I., Pierrot,
805 D., Qin, Z., Resplandy, L., Roobaert, A., Rosan, T. M., Rödenbeck, C., Schwinger, J., Smallman, T. L.,
806 Smith, S. M., Sospedra-Alfonso, R., Steinhoff, T., Sun, Q., Sutton, A. J., Séférian, R., Takao, S., Tatebe,
807 H., Tian, H., Tilbrook, B., Torres, O., Tourigny, E., Tsujino, H., Tubiello, F., van der Werf, G.,
808 Wanninkhof, R., Wang, X., Yang, D., Yang, X., Yu, Z., Yuan, W., Yue, X., Zaehle, S., Zeng, N., and Zeng,

J.: Global carbon budget 2024, Earth System Science Data, 17, 965–1039, https://doi.org/10.5194/essd-17-965-2025, 2025.

Giglio, L., Schroeder, W., and Hall, J. V.: MODIS collection 6 active fire product user's guide revision C, NASA, available at: https://modis-fire.umd.edu/files/MODIS_C6_C6.1_Active_Fire_User_Guide_C.pdf (last access: 15 August 2025), 2020.

Giglio, L., van der Werf, G. R., Randerson, J. T., Collatz, G. J., and Kasibhatla, P.: Global estimation of burned area using MODIS active fire observations, Atmospheric Chemistry and Physics, 6, 957–974, https://doi.org/10.5194/acp-6-957-2006, 2006.

Hantson, S., Padilla, M., Corti, D., and Chuvieco, E.: Strengths and weaknesses of MODIS hotspots to characterize global fire occurrence, Remote Sensing of Environment, 131, 152–159, https://doi.org/10.1016/j.rse.2012.12.004, 2013.

Hoelzemann, J. J., Schultz, M. G., Brasseur, G. P., Granier, C., and Simon, M.: Global wildland fire emission model (GWEM): Evaluating the use of global area burnt satellite data, Journal of Geophysical Research: Atmospheres, 109, https://doi.org/10.1029/2003JD003666, 2004.

Ichoku, C. and Ellison, L.: Global top-down smoke-aerosol emissions estimation using satellite fire radiative power measurements, Atmospheric Chemistry and Physics, 14, 6643–6667, https://doi.org/10.5194/acp-14-6643-2014, 2014.

Ichoku, C. and Kaufman, Y. J.: A method to derive smoke emission rates from MODIS fire radiative energy measurements, IEEE Transactions on Geoscience and Remote Sensing, 43, 2636–2649, https://doi.org/10.1109/TGRS.2005.857328, 2005.

Ito, A. and Penner, J. E.: Global estimates of biomass burning emissions based on satellite imagery for the year 2000, Journal of Geophysical Research: Atmospheres, 109, https://doi.org/10.1029/2003JD004423, 2004.

Jain, P., Barber, Q. E., Taylor, S. W., Whitman, E., Castellanos Acuna, D., Boulanger, Y., Chavardès, R. D., Chen, J., Englefield, P., Flannigan, M., Girardin, M. P., Hanes, C. C., Little, J., Morrison, K., Skakun, R. S., Thompson, D. K., Wang, X., and Parisien, M.-A.: Drivers and impacts of the record-breaking 2023 wildfire season in canada, Nature Communications, 15, 6764, https://doi.org/10.1038/s41467-024-51154-7, 2024.

838 Jen, C. N., Hatch, L. E., Selimovic, V., Yokelson, R. J., Weber, R., Fernandez, A. E., Kreisberg, N. M.,
839 Barsanti, K. C., and Goldstein, A. H.: Speciated and total emission factors of particulate organics from
840 burning western US wildland fuels and their dependence on combustion efficiency, Atmospheric
841 Chemistry and Physics, 19, 1013–1026, https://doi.org/10.5194/acp-19-1013-2019, 2019.
842 Jones, M. W., Abatzoglou, J. T., Veraverbeke, S., Andela, N., Lasslop, G., Forkel, M., Smith, A. J. P.,
843 Burton, C., Betts, R. A., van der Werf, G. R., Sitch, S., Canadell, J. G., Santín, C., Kolden, C., Doerr, S.
844 H., and Le Quéré, C.: Global and regional trends and drivers of fire under climate change, Reviews of
845 Geophysics, 60, e2020RG000726, https://doi.org/10.1029/2020RG000726, 2022.
846 Justice, C. O., Giglio, L., Korontzi, S., Owens, J., Morisette, J. T., Roy, D., Descloitres, J., Alleaume, S.,
847 Petitcolin, F., and Kaufman, Y.: The MODIS fire products, Remote Sensing of Environment, 83, 244–
848 262, https://doi.org/10.1016/S0034-4257(02)00076-7, 2002.
849 Kaiser, J. W., Heil, A., Andreae, M. O., Benedetti, A., Chubarova, N., Jones, L., Morcrette, J.-J., Razinger,
850 M., Schultz, M. G., Suttie, M., and van der Werf, G. R.: Biomass burning emissions estimated with a
851 global fire assimilation system based on observed fire radiative power, Biogeosciences, 9, 527–554,
852 https://doi.org/10.5194/bg-9-527-2012, 2012.
853 Kaiser, J. W., Holmedal, D. G., Ytre-Eide, M. A., and de Jong, M.: GFAS4HTAP vegetation fire
854 emissions 2003-2023, Zenodo [data set], https://doi.org/10.5281/zenodo.15721463, 2023.
855 Karanasiou, A., Alastuey, A., Amato, F., Renzi, M., Stafoggia, M., Tobias, A., Reche, C., Forastiere, F.,
856 Gumy, S., Mudu, P., and Querol, X.: Short-term health effects from outdoor exposure to biomass burning
857 emissions: A review, Science of The Total Environment, 781, 146739,
858 https://doi.org/10.1016/j.scitotenv.2021.146739, 2021.
859 Keeling, H. C. and Phillips, O. L.: The global relationship between forest productivity and biomass,
860 Global Ecology and Biogeography, 16, 618–631, https://doi.org/10.1111/j.1466-8238.2007.00314.x,
861 2007.
862 Koss, A. R., Sekimoto, K., Gilman, J. B., Selimovic, V., Coggon, M. M., Zarzana, K. J., Yuan, B., Lerner,
863 B. M., Brown, S. S., Jimenez, J. L., Krechmer, J., Roberts, J. M., Warneke, C., Yokelson, R. J., and de
864 Gouw, J.: Non-methane organic gas emissions from biomass burning: Identification, quantification, and
865 emission factors from PTR-ToF during the FIREX 2016 laboratory experiment, Atmospheric Chemistry
866 and Physics, 18, 3299–3319, https://doi.org/10.5194/acp-18-3299-2018, 2018.

867 Koster, R. D., Darmenov, A. S., and da Silva, A. M.: The quick fire emissions dataset (QFED):
868 Documentation of versions 2.1, 2.2 and 2.4: technical report series on global modeling and data
869 assimilation - volume 38, NASA, available at: https://ntrs.nasa.gov/citations/20180005253 (last access:
870 15 August 2025), 2015.
871 Letu, H., Ma, R., Nakajima, T. Y., Shi, C., Hashimoto, M., Nagao, T. M., Baran, A. J., Nakajima, T., Xu,
872 J., Wang, T., Tana, G., Bilige, S., Shang, H., Chen, L., Ji, D., Lei, Y., Wei, L., Zhang, P., Li, J., Li, L.,
873 Zheng, Y., Khatri, P., and Shi, J.: Surface solar radiation compositions observed from himawari-8/9 and
874 fengyun-4 series, Bulletin of the American Meteorological Society, 104, E1839–E1856,
875 https://doi.org/10.1175/BAMS-D-22-0154.1, 2023.
876 Li, K., Zheng, F., Cheng, L., Zhang, T., and Zhu, J.: Record-breaking global temperature and crises with
877 strong El Niño in 2023–2024, The Innovation Geoscience, 1, 100030, doi:10.59717/j.xinn-
878 geo.2023.100030, 2023.
879 Liu, T., Mickley, L. J., Marlier, M. E., DeFries, R. S., Khan, M. F., Latif, M. T., and Karambelas, A.:
880 Diagnosing spatial biases and uncertainties in global fire emissions inventories: Indonesia as regional
881 case study, Remote Sensing of Environment, 237, 111557, https://doi.org/10.1016/j.rse.2019.111557,
882 2020.
883 Liu, X. and Yin, S.: Multi-ensemble Biomass-burning Emissions Inventory (MBEI)_v1.0, Zenodo [data
884 set], https://doi.org/10.5281/zenodo.18104830, 2025.
885 Liu, Y., Chen, J., Shi, Y., Zheng, W., Shan, T., and Wang, G.: Global emissions inventory from open
886 biomass burning (GEIOBB): Utilizing fengyun-3D global fire spot monitoring data, Earth System
887 Science Data, 16, 3495–3515, https://doi.org/10.5194/essd-16-3495-2024, 2024.
888 Liu, Y., Gong, W., Xing, Y., Hu, X., and Gong, J.: Estimation of the forest stand mean height and
889 aboveground biomass in northeast China using SAR sentinel-1B, multispectral sentinel-2A, and DEM
890 imagery, ISPRS Journal of Photogrammetry and Remote Sensing, 151, 277–289,
891 https://doi.org/10.1016/j.isprsjprs.2019.03.016, 2019.
892 Longo, K. M., Freitas, S. R., Andreae, M. O., Setzer, A., Prins, E., and Artaxo, P.: The coupled aerosol
893 and tracer transport model to the brazilian developments on the regional atmospheric modeling system
894 (CATT-BRAMS) – part 2: Model sensitivity to the biomass burning inventories, Atmospheric Chemistry
895 and Physics, 10, 5785–5795, https://doi.org/10.5194/acp-10-5785-2010, 2010.

Luo, B., Xiao, C., Luo, D., Fu, Q., Chen, D., Zhang, Q., Ge, Y., and Diao, Y.: Atmospheric and oceanic drivers behind the 2023 canadian wildfires, Communications Earth & Environment, 6, 446, https://doi.org/10.1038/s43247-025-02387-x, 2025.

Mann, H. B.: Nonparametric tests against trend, Econometrica, 13, 245–259, https://doi.org/10.2307/1907187, 1945.

Mariani, M., Fletcher, M.-S., Holz, A., and Nyman, P.: ENSO controls interannual fire activity in southeast australia, Geophysical Research Letters, 43, 10891–10900, https://doi.org/10.1002/2016GL070572, 2016.

Matthias, V., Arndt, Jan A., Aulinger, Armin, Bieser, Johannes, Denier van der Gon, Hugo, Kranenburg, Richard, Kuenen, Jeroen, Neumann, Daniel, Pouliot, George, and Quante, M.: Modeling emissions for three-dimensional atmospheric chemistry transport models, Journal of the Air & Waste Management Association, 68, 763–800, https://doi.org/10.1080/10962247.2018.1424057, 2018.

Mieville, A., Granier, C., Liousse, C., Guillaume, B., Mouillot, F., Lamarque, J.-F., Grégoire, J.-M., and Pétron, G.: Emissions of gases and particles from biomass burning during the 20th century using satellite data and an historical reconstruction, Atmospheric Environment, 44, 1469–1477, https://doi.org/10.1016/j.atmosenv.2010.01.011, 2010.

Morton, D. C., Le Page, Y., DeFries, R., Collatz, G. J., and Hurtt, G. C.: Understorey fire frequency and the fate of burned forests in southern Amazonia, Philosophical Transactions of the Royal Society B: Biological Sciences, 368, 20120163, https://doi.org/10.1098/rstb.2012.0163, 2013.

N'Datchoh, T. E., Liousse, C., Roblou, L., and N'Dri, A. B.: Biomass burning over africa: How to explain the differences observed between the different emission inventories?, Atmosphere, 16, 440, https://doi.org/10.3390/atmos16040440, 2025.

NASA VIIRS Land Science Team: VIIRS (NOAA-21/JPSS-2) I band 375 m active fire product NRT (vector data), NASA FIRMS [data set], https://doi.org/10.5067/FIRMS/MODIS/MCD14DL.NRT.0061, 2021.

Pan, X., Ichoku, C., Chin, M., Bian, H., Darmenov, A., Colarco, P., Ellison, L., Kucsera, T., da Silva, A., Wang, J., Oda, T., and Cui, G.: Six global biomass burning emission datasets: Intercomparison and application in one global aerosol model, Atmospheric Chemistry and Physics, 20, 969–994, https://doi.org/10.5194/acp-20-969-2020, 2020.

Pellegrini, A. F. A., Ahlström, A., Hobbie, S. E., Reich, P. B., Nieradzik, L. P., Staver, A. C., Scharenbroch, B. C., Jumpponen, A., Anderegg, W. R. L., Randerson, J. T., and Jackson, R. B.: Fire frequency drives decadal changes in soil carbon and nitrogen and ecosystem productivity, Nature, 553, 194–198, https://doi.org/10.1038/nature24668, 2018.

Pereira, G., Siqueira, R., Rosário, N. E., Longo, K. L., Freitas, S. R., Cardozo, F. S., Kaiser, J. W., and Wooster, M. J.: Assessment of fire emission inventories during the south American biomass burning analysis (SAMBBA) experiment, Atmospheric Chemistry and Physics, 16, 6961–6975, https://doi.org/10.5194/acp-16-6961-2016, 2016.

Raich, J. W., Russell, A. E., Kitayama, K., Parton, W. J., and Vitousek, P. M.: Temperature influences carbon accumulation in moist tropical forests, Ecology, 87, 76–87, https://doi.org/10.1890/05-0023, 2006.

Ramanathan, V. and Carmichael, G.: Global and regional climate changes due to black carbon, Nature Geoscience, 1, 221–227, https://doi.org/10.1038/ngeo156, 2008.

Reid, J. S., Koppmann, R., Eck, T. F., and Eleuterio, D. P.: A review of biomass burning emissions part II: Intensive physical properties of biomass burning particles, Atmospheric Chemistry and Physics, 5, 799–825, https://doi.org/10.5194/acp-5-799-2005, 2005.

Rein, G. and Huang, X.: Smouldering wildfires in peatlands, forests and the Arctic: Challenges and perspectives, Current Opinion in Environmental Science & Health, 24, 100296, https://doi.org/10.1016/j.coesh.2021.100296, 2021.

Rodríguez-Fernández, N. J., Mialon, A., Mermoz, S., Bouvet, A., Richaume, P., Al Bitar, A., Al-Yaari, A., Brandt, M., Kaminski, T., Le Toan, T., Kerr, Y. H., and Wigneron, J.-P.: An evaluation of SMOS L-band vegetation optical depth (L-VOD) data sets: High sensitivity of L-VOD to above-ground biomass in africa, Biogeosciences, 15, 4627–4645, https://doi.org/10.5194/bg-15-4627-2018, 2018.

Running, S. and Zhao, M.: MODIS/aqua net primary production gap-filled yearly L4 global 500m SIN grid V061, NASA Land Processes Distributed Active Archive Center (LP DAAC) [data set], https://doi.org/10.5067/MODIS/MYD17A3HGF.061, 2021.

Santoro, M. and Cartus, O.: ESA biomass climate change initiative (biomass_cci): Global datasets of forest above-ground biomass for the years 2010, 2015, 2016, 2017, 2018, 2019, 2020 and 2021, v5.01 (5.01), Centre for Environmental Data Analysis (CEDA) [data set], https://doi.org/10.5285/bf535053562141c6bb7ad831f5998d77, 2024.

954 Santoro, M.: GlobBiomass - global datasets of forest biomass, PANGAEA [data set],
955 https://doi.org/10.1594/PANGAEA.894711, 2018.
956 Seiler, W. and Crutzen, P. J.: Estimates of gross and net fluxes of carbon between the biosphere and the
957 atmosphere from biomass burning, Climatic Change, 2, 207–247, https://doi.org/10.1007/BF00137988,
958 1980.
959 Sen, P. K.: Estimates of the regression coefficient based on kendall's tau, Journal of the American
960 Statistical Association, 63, 1379–1389, https://doi.org/10.1080/01621459.1968.10480934, 1968.
961 Senande-Rivera, M., Insua-Costa, D., and Miguez-Macho, G.: Spatial and temporal expansion of global
962 wildland fire activity in response to climate change, Nature Communications, 13, 1208,
963 https://doi.org/10.1038/s41467-022-28835-2, 2022.
964 Shi, C., Letu, H., et al.: Near-global monitoring of surface solar radiation through the construction of a
965 geostationary satellite network observation system, The Innovation, 6, 100876,
966 https://doi.org/10.1016/j.xinn.2025.100876, 2025.
967 Shi, Y. and Matsunaga, T.: Temporal comparison of global inventories of CO_2 emissions from biomass
968 burning during 2002–2011 derived from remotely sensed data, Environmental Science and Pollution
969 Research, 24, 16905–16916, https://doi.org/10.1007/s11356-017-9141-z, 2017.
970 Shi, Y., Matsunaga, T., Saito, M., Yamaguchi, Y., and Chen, X.: Comparison of global inventories of CO_2
971 emissions from biomass burning during 2002–2011 derived from multiple satellite products,
972 Environmental Pollution, 206, 479–487, https://doi.org/10.1016/j.envpol.2015.08.009, 2015.
973 Silva, S. S. da, Fearnside, P. M., Graça, P. M. L. de A., Brown, I. F., Alencar, A., and Melo, A. W. F. de:
974 Dynamics of forest fires in the southwestern amazon, Forest Ecology and Management, 424, 312–322,
975 https://doi.org/10.1016/j.foreco.2018.04.041, 2018.
976 Sofan, P., Bruce, D., Jones, E., and Marsden, J.: Detection and validation of tropical peatland flaming
977 and smouldering using Landsat-8 SWIR and TIRS bands, Remote Sensing, 11, 465,
978 https://doi.org/10.3390/rs11040465, 2019.
979 Stroppiana, D., Brivio, P. A., Grégoire, J.-M., Liousse, C., Guillaume, B., Granier, C., Mieville, A., Chin,
980 M., and Pétron, G.: Comparison of global inventories of CO emissions from biomass burning derived
981 from remotely sensed data, Atmospheric Chemistry and Physics, 10, 12173–12189,
982 https://doi.org/10.5194/acp-10-12173-2010, 2010.

983 Su, M., Shi, Y., Yang, Y., and Guo, W.: Impacts of different biomass burning emission inventories:
984 Simulations of atmospheric CO_2 concentrations based on GEOS-chem, Science of The Total
985 Environment, 876, 162825, https://doi.org/10.1016/j.scitotenv.2023.162825, 2023.
986 Teets, A., Moore, D., Alexander, M., Blanken, P., Bohrer, G., Burns, S., Carbone, M., Ducey, M., Fraver,
987 S., Gough, C., Hollinger, D., Koch, G., Kolb, T., Munger, J., Novick, K., Ollinger, S., Ouimette, A.,
988 Pederson, N., Ricciuto, D., and Richardson, A.: Coupling of tree growth and photosynthetic carbon
989 uptake across six North American forests, Journal of Geophysical Research: Biogeosciences, 127,
990 e2021JG006690, https://doi.org/10.1029/2021JG006690, 2022.
991 Touma, D., Stevenson, S., Lehner, F., and Coats, S.: Human-driven greenhouse gas and aerosol emissions
992 cause distinct regional impacts on extreme fire weather, Nature Communications, 12, 212,
993 https://doi.org/10.1038/s41467-020-20570-w, 2021.
994 Tyukavina, A., Potapov, P., Hansen, M. C., Pickens, A. H., Stehman, S. V., Turubanova, S., Parker, D.,
995 Zalles, V., Lima, A., Kommareddy, I., Song, X.-P., Wang, L., and Harris, N.: Global trends of forest loss
996 due to fire from 2001 to 2019, Frontiers in Remote Sensing, 3, 825190,
997 https://doi.org/10.3389/frsen.2022.825190, 2022.
998 van der Velde, I. R., van der Werf, G. R., Houweling, S., Eskes, H. J., Veefkind, J. P., Borsdorff, T., and
999 Aben, I.: Biomass burning combustion efficiency observed from space using measurements of CO and
1000 NO_2 by the TROPOspheric monitoring instrument (TROPOMI), Atmospheric Chemistry and Physics,
1001 21, 597–616, https://doi.org/10.5194/acp-21-597-2021, 2021.
1002 van der Werf, G. R., Morton, D. C., DeFries, R. S., Giglio, L., Randerson, J. T., Collatz, G. J., and
1003 Kasibhatla, P. S.: Estimates of fire emissions from an active deforestation region in the southern amazon
1004 based on satellite data and biogeochemical modelling, Biogeosciences, 6, 235–249,
1005 https://doi.org/10.5194/bg-6-235-2009, 2009.
1006 Vadrevu, K. and Lasko, K.: Intercomparison of MODIS AQUA and VIIRS I-band fires and emissions in
1007 an agricultural landscape — implications for air pollution research, Remote Sensing, 10, 978,
1008 https://doi.org/10.3390/rs10070978, 2018.
1009 van der Werf, G. R., Randerson, J. T., Giglio, L., Collatz, G. J., Kasibhatla, P. S., and Arellano, A. F. J.:
1010 Interannual variability in global biomass burning emissions from 1997 to 2004, Atmospheric Chemistry
1011 and Physics, 6, 3423–3441, https://doi.org/10.5194/acp-6-3423-2006, 2006.

van der Werf, G. R., Randerson, J. T., Giglio, L., van Leeuwen, T. T., Chen, Y., Rogers, B. M., Mu, M., van Marle, M. J. E., Morton, D. C., Collatz, G. J., Yokelson, R. J., and Kasibhatla, P. S.: Global fire emissions estimates during 1997–2016, Earth System Science Data, 9, 697–720, https://doi.org/10.5194/essd-9-697-2017, 2017.

van Leeuwen, T. T., Peters, W., Krol, M. C., and van der Werf, G. R.: Dynamic biomass burning emission factors and their impact on atmospheric CO mixing ratios, Journal of Geophysical Research: Atmospheres, 118, 6797–6815, https://doi.org/10.1002/jgrd.50478, 2013.

van Wees, D., van der Werf, G. R., Randerson, J. T., Andela, N., Chen, Y., and Morton, D. C.: The role of fire in global forest loss dynamics, Global Change Biology, 27, 2377–2391, https://doi.org/10.1111/gcb.15591, 2021.

Vermote, E., Ellicott, E., Dubovik, O., Lapyonok, T., Chin, M., Giglio, L., and Roberts, G. J.: An approach to estimate global biomass burning emissions of organic and black carbon from MODIS fire radiative power, Journal of Geophysical Research: Atmospheres, 114, D18205, https://doi.org/10.1029/2008JD011188, 2009.

Vernooij, R., Eames, T., Russell-Smith, J., Yates, C., Beatty, R., Evans, J., Edwards, A., Ribeiro, N., Wooster, M., Strydom, T., Giongo, M. V., Borges, M. A., Menezes Costa, M., Barradas, A. C. S., van Wees, D., and Van der Werf, G. R.: Dynamic savanna burning emission factors based on satellite data using a machine learning approach, Earth System Dynamics, 14, 1039–1064, https://doi.org/10.5194/esd-14-1039-2023, 2023.

Wang, F., Harindintwali, J. D., Wei, K., Shan, Y., Mi, Z., Costello, M. J., Grunwald, S., Feng, Z., Wang, F., Guo, Y., Wu, X., Kumar, P., Kästner, M., Feng, X., Kang, S., Liu, Z., Fu, Y., Zhao, W., Ouyang, C., Shen, J., Wang, H., Chang, S. X., Evans, D. L., Wang, R., Zhu, C., Xiang, L., Rinklebe, J., Du, M., Huang, L., Bai, Z., Li, S., Lal, R., Elsner, M., Wigneron, J.-P., Florindo, F., Jiang, X., Shaheen, S. M., Zhong, X., Bol, R., Vasques, G. M., Li, X., Pfautsch, S., Wang, M., He, X., Agathokleous, E., Du, H., Yan, H., Kengara, F. O., Brahushi, F., Long, X.-E., Pereira, P., Ok, Y. S., Rillig, M. C., Jeppesen, E., Barceló, D., Yan, X., Jiao, N., Han, B., Schäffer, A., Chen, J. M., Zhu, Y., Cheng, H., Amelung, W., Spötl, C., Zhu, J., and Tiedje, J. M.: Climate change: strategies for mitigation and adaptation, The Innovation Geoscience, 1, 100015, doi:10.59717/j.xinn-geo.2023.100015, 2023.

Whitburn, S., Damme, M. V., Clarisse, L., Turquety, S., Clerbaux, C., and Coheur, P.-F.: Doubling of annual ammonia emissions from the peat fires in indonesia during the 2015 el niño, Geophysical Research Letters, 43, 11007–11014, https://doi.org/10.1002/2016GL070620, 2016.

Whittaker, R. H. and Likens, G. E.: Carbon in the biota, in: Carbon and the Biosphere, edited by: Woodwell, G. M. and Pecan, E. V., U.S. Atomic Energy Commission, Washington, D.C., 281–302, 1972.

Wiedinmyer, C., Kimura, Y., McDonald-Buller, E. C., Emmons, L. K., Buchholz, R. R., Tang, W., Seto, K., Joseph, M. B., Barsanti, K. C., Carlton, A. G., and Yokelson, R.: The fire inventory from NCAR version 2.5: An updated global fire emissions model for climate and chemistry applications, Geoscientific Model Development, 16, 3873–3891, https://doi.org/10.5194/gmd-16-3873-2023, 2023.

Wiedinmyer, C., Quayle, B., Geron, C., Belote, A., McKenzie, D., Zhang, X., O'Neill, S., and Wynne, K. K.: Estimating emissions from fires in north America for air quality modeling, Atmospheric Environment, 40, 3419–3432, https://doi.org/10.1016/j.atmosenv.2006.02.010, 2006.

Wiggins, E. B., Andrews, A., Sweeney, C., Miller, J. B., Miller, C. E., Veraverbeke, S., Commane, R., Wofsy, S., Henderson, J. M., and Randerson, J. T.: Boreal forest fire CO and CH_4 emission factors derived from tower observations in alaska during the extreme fire season of 2015, Atmospheric Chemistry and Physics, 21, 8557–8574, https://doi.org/10.5194/acp-21-8557-2021, 2021.

Wiggins, E. B., Czimczik, C. I., Santos, G. M., Chen, Y., Xu, X., Holden, S. R., Randerson, J. T., Harvey, C. F., Kai, F. M., and Yu, L. E.: Smoke radiocarbon measurements from Indonesian fires provide evidence for burning of millennia-aged peat, Proceedings of the National Academy of Sciences, 115, 12419–12424, https://doi.org/10.1073/pnas.1806003115, 2018.

Williams, J. E., Weele, M. van, Velthoven, P. F. J. van, Scheele, M. P., Liousse, C., and Werf, G. R. van der: The impact of uncertainties in african biomass burning emission estimates on modeling global air quality, long range transport and tropospheric chemical lifetimes, Atmosphere, 3, 132–163, https://doi.org/10.3390/atmos3010132, 2012.

Wooster, M. J., Roberts, G., Perry, G. L. W., and Kaufman, Y. J.: Retrieval of biomass combustion rates and totals from fire radiative power observations: FRP derivation and calibration relationships between biomass consumption and fire radiative energy release, Journal of Geophysical Research: Atmospheres, 110, D24310, https://doi.org/10.1029/2005JD006318, 2005.

Yin, S.: Decadal trends of MERRA-estimated $PM_{2.5}$ concentrations in East Asia and potential exposure from 1990 to 2019, Atmospheric Environment, 264, 118690, doi:10.1016/j.atmosenv.2021.118690, 2021.

Yin, S., Shi, C., Letu, H., Ito, A., Shang, H., Ji, D., Li, L., Bilige, S., Nie, T., Yi, K., Guo, M., Sun, Z., and Li, A.: Reconstruction of $PM_{2.5}$ concentrations in east asia on the basis of a wide–deep ensemble machine learning framework and estimation of the potential exposure level from 1981 to 2020, Engineering, 49, 225–237, https://doi.org/10.1016/j.eng.2024.09.025, 2025.

Yin, S., Wang, X., Guo, M., Santoso, H., and Guan, H.: The abnormal change of air quality and air pollutants induced by the forest fire in sumatra and borneo in 2015, Atmospheric Research, 243, 105027, https://doi.org/10.1016/j.atmosres.2020.105027, 2020a.

Yin, S.: Effect of biomass burning on premature mortality associated with long-term exposure to $PM_{2.5}$ in Equatorial Asia, Journal of Environmental Management, 330, 117154, https://doi.org/10.1016/j.jenvman.2022.117154, 2023.

Yin, S.: Exploring the relationships between ground-measured particulate matter and satellite-retrieved aerosol parameters in China, Environmental Science and Pollution Research, 29, 44348–44363, doi:10.1007/s11356-022-19049-6, 2022.

Yin, Y., Bloom, A. A., Worden, J., Saatchi, S., Yang, Y., Williams, M., Liu, J., Jiang, Z., Worden, H., Bowman, K., Frankenberg, C., and Schimel, D.: Fire decline in dry tropical ecosystems enhances decadal land carbon sink, Nature Communications, 11, 1900, https://doi.org/10.1038/s41467-020-15852-2, 2020b.

Zhang, F., Wang, J., Ichoku, C., Hyer, E. J., Yang, Z., Ge, C., Su, S., Zhang, X., Kondragunta, S., and Kaiser, J. W.: Sensitivity of mesoscale modeling of smoke direct radiative effect to the emission inventory: A case study in northern sub-saharan african region, Environmental Research Letters, 9, 075002, https://doi.org/10.1088/1748-9326/9/7/075002, 2014.

Zhang, Y., Albinet, A., Petit, J.-E., Jacob, V., Chevrier, F., Gille, G., Pontet, S., Chrétien, E., Dominik-Sègue, M., Levigoureux, G., Močnik, G., Gros, V., Jaffrezo, J.-L., and Favez, O.: Substantial brown carbon emissions from wintertime residential wood burning over france, Science of The Total Environment, 743, 140752, https://doi.org/10.1016/j.scitotenv.2020.140752, 2020.

Zheng, B., Ciais, P., Chevallier, F., Chuvieco, E., Chen, Y., and Yang, H.: Increasing forest fire emissions despite the decline in global burned area, Science Advances, 7, eabh2646, https://doi.org/10.1126/sciadv.abh2646, 2021.

Zheng, B., Ciais, P., Chevallier, F., Yang, H., Canadell, J. G., Chen, Y., van der Velde, I. R., Aben, I., Chuvieco, E., Davis, S. J., Deeter, M., Hong, C., Kong, Y., Li, H., Li, H., Lin, X., He, K., and Zhang, Q.:

1100 Record-high CO_2 emissions from boreal fires in 2021, Science, 379, 912–917,
1101 https://doi.org/10.1126/science.ade0805, 2023.